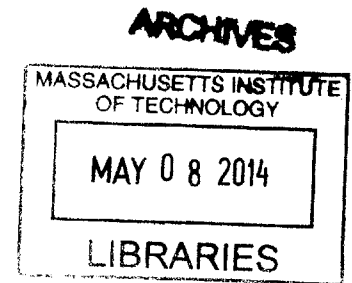# Investigation of sub-bandgap absorption in iron pyrite: optical and electrical measurements

by

Rupak Chakraborty

A.B., Physics
Harvard University (2010)

Submitted to the Department of Mechanical Engineering
in partial fulfillment of the requirements for the degree of

Master of Science in Mechanical Engineering

at the

MASSACHUSETTS INSTITUTE OF TECHNOLOGY

February 2014

© Massachusetts Institute of Technology 2014. All rights reserved.

Author . . . .
Department of Mechanical Engineering
January 17, 2014

Certified by. . . . .
Tonio Buonassisi
Associate Professor of Mechanical Engineering
Thesis Supervisor

Accepted by . . . .
David Hardt, Professor of Mechanical Engineering
Chairman, Department Committee on Graduate Theses

Investigation of sub-bandgap absorption in iron pyrite: optical and electrical measurements

by

Rupak Chakraborty

Submitted to the Department of Mechanical Engineering
on January 17, 2014, in partial fulfillment of the
requirements for the degree of
Master of Science in Mechanical Engineering

Abstract

We investigate sub-bandgap absorption in pyrite FeS_2 single-crystals, using both natural and synthetic crystals. Both types of crystals show non-negligible magnitudes of sub-bandgap absorption. To test whether the origin of the residual sub-bandgap absorption is partially due to a lower bulk bandgap than previously thought, we conduct temperature-dependent electrical measurements on natural and synthetic crystals. Unlike previous measurements on pyrite, our electrical measurements are done in a sulfur atmosphere to avoid FeS formation. Using conductivity data in the intrinsic regime along with extrapolated Hall mobility data, the extracted bandgap is more than 0.1 eV lower than the literature value of 0.95 eV. However, higher-temperature Hall data are needed to gain a more reliable bandgap estimate.

Thesis Supervisor: Tonio Buonassisi
Title: Associate Professor of Mechanical Engineering

Acknowledgments

In these few paragraphs, I face the impossible challenge of expressing in words my deep gratitude towards those who contributed to the completion of this thesis.

This work would not be possible without the support and guidance of my advisor, Professor Tonio Buonassisi, over the past two years. Under his mentorship, I have learned an incredible amount about photovoltaics, about the importance of collaboration, about developing worthy research questions, and about becoming a well-rounded scientist. In addition to his direct mentorship, I would also like to thank him for assembling the phenomenal group of students, post-docs, and staff that comprise the PVLab. The collaborative environment that Tonio has created has played an immense role in the advancement of this research project.

I would like to thank the three main collaborators on this project. Thanks to Will Herbert for providing precious synthetic pyrite samples, for help with preliminary optical and electrical measurements, for help with the design and prototyping of the sample chamber, and for various fruitful discussions regarding experimental details. Critical to the start of this project were Predrag Lazić and Rickard Armiento, whose theoretical calculations prompted a closer look at the electrical bandgap of pyrite. Thanks to them for helpful in-depth discussions about the unique band structure of pyrite.

I am deeply indebted to Renee Sher, who mentored me on the various experimental intricacies of Hall measurements, trained me on the Hall cryostat setup in the Mazur lab at Harvard, and supervised preliminary Hall measurements for this research project. Aside from being a pleasure to work with, Renee helped me gain an intuition for interpreting Hall measurements which was critical to the completion of this thesis.

I owe everyone in the PVLab for their support throughout this project, not just through their assistance in the lab, but also through their friendship. A special thanks is in order for Mark Winkler, Joe Sullivan, Christie Simmons, Rafael Jaramillo, and Austin Akey, whose direct mentorship on optical and electrical measurements,

discussions about experimental methods, and advice on sample chamber design were extremely helpful in the execution of this project. I would also like to thank the Central Machine Shop at MIT, the Center for Materials Science and Engineering at MIT, and the Center for Nanoscale Systems at Harvard for their facilities used in fabrication and experimentation.

Finally, the past two years are impossible to imagine without my family and friends, whose loving support reaches far beyond the lab.

Contents

List of Figures

List of Tables

THIS PAGE INTENTIONALLY LEFT BLANK

Chapter 1

Introduction

Considering the impact of fossil fuels on climate change and the increasing global demand for energy, there is an ever-growing need to adopt renewable, clean, and cost-effective energy sources. Of all the energy sources we can harvest on earth, solar irradiation is by far the most abundant [1]. Despite its enormous potential, solar energy comprises less than 0.3% of energy production in the United States [2]. The main barrier preventing the widespread adoption of photovoltaic technology is the relatively high cost per peak watt (W_p) compared to conventional energy sources.

Over the past decade, significant progress has been made in thin-film photovoltaic technology because of its cost-advantage over silicon-based photovoltaics. In particular, chalcogenide-based thin-films such as $CuIn_xGa_{1-x}Se_2$ (CIGS) and CdTe have recently achieved less than $0.59/W_p$, and are still decreasing in cost [3]. Unfortunately, CIGS and CdTe use elements that are not abundant in the earth's crust, and their total production capacity is limited to 670 W [4]. In order to meet terawatt-level global energy demand, thin-film devices must be engineered to use relatively earth-abundant materials.

1.1 Iron pyrite as a solar absorber

Iron pyrite (FeS_2) has long been thought to be one of the most promising next-generation solar-absorbing materials. In addition to being earth-abundant, iron pyrite

13

has several desirable characteristics as a solar absorber material. First, iron pyrite has a large absorption coefficient, of the order 10^5 cm^{-1} at photon energies of 1-1.5 eV, allowing it to absorb 90% of sunlight in less than 100 nm of material [5]. In addition, as we will be discussing, the bandgap of pyrite is widely quoted in the literature as 0.95 eV, which is close to the optimum for a single-junction photovoltaic device [6]. These characteristics led to a large effort in pyrite solar cell research in the 80s and 90s [5]. However, the best published efficiency for a pyrite solar cell device is only 2.8% [5], paling in comparison to its theoretical maximum efficiency of 29% based on a bandgap of 0.95 eV [6].

1.2 Low V_{OC} and high sub-bandgap absorption in FeS2

While high short-circuit currents and quantum efficiencies have been reported for pyrite solar cells [5], nearly all pyrite devices in the literature have been plagued by a low open-circuit voltage (V_{OC}). For the current record-efficiency pyrite device, the V_{OC} was 187 mV, significantly lower than the theoretical maximum of $\sim$500 mV assuming a bandgap of 0.95 eV. Recently, there has been a renewed interest in understanding the mechanisms responsible for the low V_{OC} of FeS$_2$ devices [7,8]. Suggestions for the underlying reasons include various defects at the surface, such as sulfur vacancies or line defects in the bulk or on the surface of pyrite [9–12]. Another popular suggestion is that the Fermi level might be pinned by intrinsic surface states [5,12–14]. Lastly, impurity phases, primarily marcasite, have been suggested to cause the low V_{OC} of pyrite devices [15]. Many of these suggestions, however, have been contested by recent theoretical computations [16,17]. That pyrite exhibits high short-circuit currents also suggests that the V_{OC} is not affected by recombination centers in the bulk [5].

In light of the shortcomings of these explanations for low V_{OC}, a recent computational study by Lazić et al. [8] suggests that the intrinsic density of states of pyrite,

rather than extrinsic defects, may be reponsible for the low V_{OC} of pyrite devices. The authors found that a low-intensity conduction band tail may exist in the bulk density of states, which lowers the fundamental bandgap to ~0.5 eV. They argue that the conduction band tail, in combination with a high density of intrinsic surface states, may explain the low V_{OC} commonly observed in pyrite solar cells. Moreover, recent measurements by scanning tunneling microscopy have shown that the intrinsic (100) surface bandgap of pyrite is indeed reduced to 0.4 eV, far less than the "accepted" bulk bandgap of 0.95 eV [18]. These findings suggest that the value of the bulk bandap of pyrite currently used in the literature may need to be re-examined. In the next section, we review attempts in the literature to measure the bulk bandgap of pyrite.

1.3   Measuring the bandgap of FeS$_2$

In general, there are not many reliable ways to measure the bulk bandgap of a material. Each method comes with a set of assumptions, and one must ensure that the assumptions are reasonable for the material of interest. In the case of pyrite, the bulk bandgap has been measured in several ways, but each method has its drawbacks.

1.3.1   Optical methods and sub-bandgap absorption

A summary of optical bandgaps extracted from absorption coefficient measurements on single-crystalline pyrite to date are shown in Table 1.1. One of the most common ways to estimate the bandgap (E_g) of a material is by measuring optical absorption. In this method, the absorption coefficient (α) is measured as function of incident photon energy ($h\nu$). As we increase photon energy, the absorption coefficient should sharply increase in the vicinity of $h\nu = E_g$, and the photon energy at which this occurs is often taken to be an estimate of the bandgap. Using this method, the bandgap of single-crystalline pyrite has been estimated as 0.9 eV - 1.6 eV [19–22]. In all cases however, significant absorption ($\alpha > 10^3$ cm^{-1}) was measured below the quoted bandgap. This "sub-bandgap" absorption was attributed to crystalline defects

in [19], but the authors did not investigate further. Henceforth, we refer to all optical absorption below the *accepted* bandgap of 0.95 eV as sub-bandgap absorption.

A better way to extract the bandgap from optical absorption is by fitting the absorption coefficient in the vicinity of the bandgap. The exact dependence of α on $h\nu$ is a function of E_g, and can be derived based on the nature of the valence to conduction band transition. Assuming parabolic bands, an $\alpha \propto (h\nu - E_g)^{1/2}$ dependence is expected for an allowed direct transition, while an $\alpha \propto (h\nu - E_g)^2$ dependence is expected for an indirect transition [23]. Thus, by fitting the absorption coefficient data, one can infer both the type of transition responsible for absorption and the value of the bandgap. Values reported for single-crystalline pyrite using this fitting procedure include 0.93 eV [24, 25] and 0.77 eV [26], both of which were obtained assuming an indirect fundamental bandgap. These values were first called into question by Ferrer *et al.* [27], who suggest that the fitting of optical absorption data may be insufficient to accurately determine the bandgap of pyrite because of the non-parabolic nature of its band edge.

Perhaps more significant, however, is that all of the studies involving fitting of optical absorption exhibited significant sub-bandgap absorption. In every case, the sub-bandgap absorption was substracted from the absorption spectra before fitting for the bandgap. Though the substraction would be justified if all of the sub-bandgap absorption were due to defects, evidence of this claim is lacking. If the sub-bandgap absorption is at least partially intrinsic to the bulk of pyrite as [8] suggests, the literature bandgaps may be severe overestimates of the fundamental bandgap of pyrite. Indeed, a thin conduction band tail which reduces the fundamental bandgap to 0.5 eV would appear as an absorption tail which could easily be attributed to defect-related absorption [8] below the accepted bandgap of 0.95 eV.

Thus, because of anomalous sub-bandgap absorption in iron pyrite, measuring the bandgap using optical absorption methods may not be reliable.

Ref.	Crystal type	Treatment of data	E_g (eV)
[19]	Natural and Synth.	α, n, k, ϵ vs. λ	0.9
[20]	Natural	α, n, k, ϵ vs. λ	0.95
[26]	Natural	$(\alpha h\nu)^n$ vs. $h\nu^*$	0.77
[21]	Natural	α, n, k, ϵ vs. λ	1.6
[25]	Natural	$(\alpha h\nu)^n$ vs. $h\nu^*$	0.93
[24]	Synthetic	$(\alpha h\nu)^n$ vs. $h\nu^*$	0.93
[22]	Synthetic	α, n, k, ϵ vs. λ	0.9

Table 1.1: Summary of optical bandgap estimates from literature. Asterisk indicates that an allowed indirect transition was assumed in calculating the bandgap.

1.3.2 Electrical methods

Another way to measure the bandgap is by temperature-dependent electrical transport measurements, as explained in Chapter 2. Temperature-dependent resistivity, Hall mobility, and Hall coefficient have been documented extensively for single-crystalline pyrite samples [22, 25, 28–38]. Of these studies, only four reach temperatures high enough to be interpreted as the intrinsic regime from which the bandgap can be extracted (see Section 2.2) [22, 25, 35–37]. A summary of the four studies which extract a bandgap from electrical measurments is shown in Table 1.2. As shown, there is a large spread in the extracted electrical bandgap. This may be due to several reasons.

First, three of the studies are based on natural crystals, which may contain a wide variety of impurity concentrations. Indeed, it has been shown that concentrations of certain elements such as Al and Si can have a significant impact on electrical properties [28]. The lack of comprehensive impurity concentration measurements for the natural crystal studies make them difficult to compare directly. One could argue that in the intrinsic regime, the effects of impurities should be masked by band-to-band transitions. However, the studies still assume that the bandgap is independent of impurity concentration, which may not be valid for high impurity concentrations in natural crystals [28].

Aside from concerns about impurity concentration, the previous electrical bandgap studies face a more important problem. Measurements of the intrinsic regime, as de-

scribed in Section 2.2, require elevated temperatures. One must ensure that the sample does not undergo a phase change at these elevated temperatures. Unfortunately, the Fe-S system contains many phases which are more iron-rich than FeS_2, the most stable of which is pyrrhotite FeS [39]. Because of the relatively high vapor pressure of sulfur, it is thermodynamically favorable for sulfur to evaporate off the surface of pyrite and form pyrrhotite at elevated temperatures. Thus, care must be taken to operate at temperatures and sulfur partial pressures for which pyrite is the most thermodynamically favorable phase. In our preliminary experiments, it was found that the degradation of the pyrite surface into pyrrhotite occurs at $\sim$ 450 K in a low vacuum ($\sim$50 torr) atmosphere, confirmed by X-ray diffraction measurements.

Despite the known possibility of secondary-phase formation, the previous measurements of the electrical bandgap did not involve a controlled atmosphere [22,25,35–37]. There are no mentions of FeS prevention except in [25], which states that surface blackening occurs at $\sim$550 K. The blackening is consistent with the appearance of FeS on the surface, but from our experience, the temperature at which FeS surface formation occurs as detectable by XRD is much lower, at $\sim$450 K. It is possible that in the case of [25], an FeS surface layer formed but was not visible as a blackened surface. Indeed, an early work by Echarri *et al.* [38] comments on the unreliability of data above 475 K due to decomposition of pyrite, probably due to a desulphation process. If FeS was forming at the sample surface as temperature increased, the temperature dependence of the measured conductivity would give a bandgap that is higher than that of pure pyrite, since FeS is more conductive than FeS_2. This would lead to over-estimating the electrical bandgap of pyrite, consistent with the proposed direction of error in previous optical bandgap measurements due to sub-bandgap absorption.

Ref.	Crystal type	Temperatures (K)	Measured quantities	E_g (eV)
[22]	Synthetic	300-645	$\rho(T)$	0.92*
[35]	Natural	300-675	$\rho(T)$	1.2*
[36,37]	Natural	300-730	$\rho(T)$, $R_H(T)$	0.73*, 0.77*
[25]	Natural	300-550	$\rho(T)$, $R_H(T)$	0.93 eV

Table 1.2: Summary of electrical bandgap estimates from literature. Asterisk indicates that the extracted bandgap was not corrected for temperature-dependence of the bandgap.

1.4 Goal of this work

We propose to investigate the phenomenon of sub-bandgap absorption in pyrite single-crystals, with the hypothesis that the sub-bandgap absorption is due in part to an overestimate of the intrinsic bulk bandgap of pyrite in the literature. We first measure the optical absorption spectra of both natural and synthetic single-crystals, comparing to literature results. We then measure the temperature-dependent electrical properties of both types of crystals in the intrinsic regime under a controlled sulfur atmosphere, with the intention of extracting the fundamental bandgap of pyrite without the sources of errors identified for similar measurements in the literature.

THIS PAGE INTENTIONALLY LEFT BLANK

Chapter 2

Measurement of electronic transport properties

2.1 Hall Effect

The Hall effect can be used to gain a wealth of information about crystalline semi-conductors. In particular, if the Hall effect is measured as a function of temperature, the dopant activation energy and material bandgap can be determined. The most general experimental setup for measuring the Hall effect is shown in Figure 2-1. A current density $J\hat{x}$ is applied to a slab of material while immersed in a magnetic field $B\hat{z}$ oriented perpendicular to the current density. The charge carriers inside the material deflect in the y direction due to the Lorentz force, and the deflection creates an opposing electrostatic force. The deflection continues until the Lorentz force exactly balances the electrostatic force in the y direction, resulting in a steady-state electrical potential V_H in the y direction.

For the geometry in Figure 2-1, the Hall voltage V_H is given by

$$V_H = R_H \frac{IB}{t}$$

where I is the current across the slab in the x direction, B is the magnitude of the magnetic field, t is the thickness of the slab, and R_H is the Hall coefficient. In the case
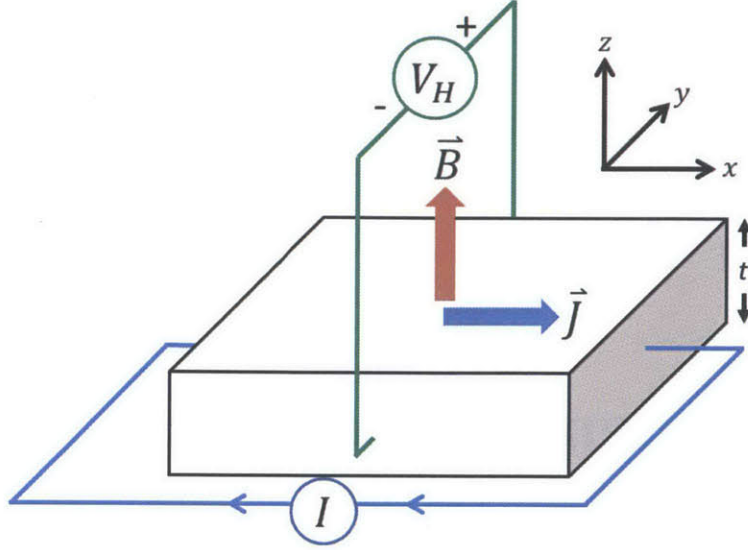
Figure 2-1: Basic Hall effect geometry. A magnetic field $B\hat{z}$ and current density $J\hat{x}$ are applied to a slab material, inducing an electrostatic potential difference in the y direction due to the balance between the Lorentz and electrostatic force on the charge carriers.

of a semiconductor, the material may contain both electron and hole charge carriers and the Hall coefficient is given by [40]

$$R_H = \frac{p\mu_h^2 - n\mu_e^2}{q(p\mu_h + n\mu_e)^2} \tag{2.1}$$

where n is the electron carrier density, p is the hole carrier density, μ_e is the electron mobility, μ_h is the hole mobility, and q is the elementary charge. There are two important limiting cases of the Hall coefficient. When $n\mu_e \gg p\mu_h$, the Hall coefficient reduces to

$$R_H \approx -\frac{1}{nq}. \tag{2.2}$$

This is typically the case for a doped n-type semiconductor at low temperature. On the other hand, when $n \approx p$, the Hall coefficient reduces to

$$R_H \approx \frac{1}{n}\left(\frac{\mu_h - \mu_e}{\mu_h + \mu_e}\right). \tag{2.3}$$

Hall effect measurements may be combined with resistivity measurements to give the

Hall mobility, defined as

$$\mu_{Hall} = \frac{1}{R_H \rho} = \frac{\sigma}{R_H} \tag{2.4}$$

where ρ is the resistivity and $\sigma = 1/\rho$ is the conductivity. In general, the conductivity can be expressed by the well known relation

$$\sigma = q(p\mu_h + n\mu_e).$$

When $n \approx p$, the conductivity and Hall mobility become

$$\sigma \approx qn(\mu_h + \mu_e) \tag{2.5}$$

and

$$\mu_{Hall} \approx \mu_h + \mu_e. \tag{2.6}$$

The above approximations found for $n \approx p$ play a critical role for describing the temperature dependence in the intrinsic regime of a semiconductor, discussed in Section 2.2.

Although the slab geometry shown in Figure1 2-1 is convenient to treat mathematically, it is rarely used in practice because it requires contact to the side faces of the sample. Therefore, other more experimentally convenient geometries have been developed. In this work, we use the Van der Pauw geometry, in which the four contacts lie on top surface of the sample near the edges. The full mathematical treatment of resistivity and Hall measurements for the Van der Pauw geometry can be found in [41]. The main advantage of this geometry is that the shape of the slab may be arbitrary, so long as the thickness of the slab is much less than span of the slab in the lateral dimensions.

2.2 Hall Effect and semiconductor statistics

In this section, we examine the temperature dependence of the carrier concentration in a semiconductor. Consider a semiconductor with bandgap E_g, donor concentration
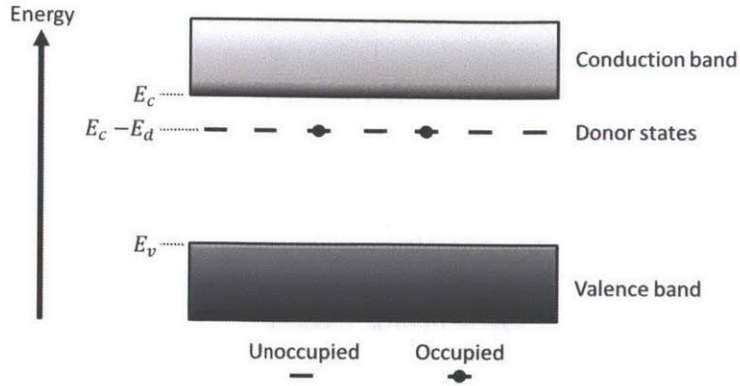
23

Figure 2-2: Simple band diagram with partially ionized donors. In the conduction and valence bands, darker shading represents higher occupancy. Adapted from [42].

N_d, donor states at energy $E_c - E_d$, and acceptor concentration zero. A representative energy band diagram is shown in Figure 2-2. Additionally, let the intrinsic carrier concentration n_i be much less than N_d. The carrier concentration as a function of temperature can be derived using Fermi-Dirac statistics for this case, and the treatment can be found elsewhere [42]. There are typically three temperature regimes, each having a distinct carrier concentration dependence on temperature. At moderate temperatures for which $k_b T \gg E_d$ but $k_b T \ll E_g$, the carrier concentration becomes

$$n(T) = N_d$$

as we expect, since all donors are ionized and the contribution of carriers from donor levels dominates over the contribution from the valence band (assuming $n_i \ll N_d$). This regime is referred to as the extrinsic regime.

As the sample is cooled, the carrier concentration decreases as electrons relax into the donor levels. In this "freeze-out" regime, the carrier concentration can be approximated by [42]

$$n(T) \approx \sqrt{\beta N_c N_d} \exp\left(-\frac{E_d}{2k_b T}\right).$$

Therefore, a plot of $\log(n)$ versus $1/T$, referred to as an Arrhenius plot, will appear linear with slope $E_d/2$ in this regime.

24

On the contrary, as the sample is heated such that $k_b T \sim E_g$, the carrier concentration will begin to increase due to the emptying of valence band states. Eventually, the contribution of carriers from the valence band will dominate over the contribution from ionized donors. For these temperatures, called the intrinsic regime, we can ignore the donor contribution, and the carrier concentration can be expressed in general terms as

$$n(T) = \int_{E_c}^{\infty} f(E) \cdot g(E) \, dE.$$

Here, E_c is the conduction minimum, the occupation probability $f(E)$ is given by the Fermi function

$$f(E) = \frac{1}{1 + \exp\left(\frac{E - E_F}{k_b T}\right)},$$

and $g(E)$ is the conduction band density of states, which if we approximate as parabolic can be expressed as

$$g(E) = 4\pi \left(\frac{2m_e^*}{h^2}\right)^{3/2} (E - E_c)^{1/2},$$

where E_F is the Fermi level, m_e^* is the effective mass of an electron near the conduction band minimum and h is Planck's constant. Substituting these expressions yields

$$n(T, \eta) = N_c(T) \mathcal{F}_{1/2}(\eta)$$

where $\mathcal{F}_{1/2}$ is the Fermi-Dirac integral, and we have defined

$$N_c(T) \equiv 2 \left(\frac{2\pi m_e^* k_b T}{h^2}\right)^{3/2} \quad , \quad \eta \equiv \frac{E_F - E_c}{k_b T}.$$

For a non-degenerate semiconductor, the Fermi-Dirac integral can be approximated as $\mathcal{F}_{1/2} = \exp(\eta)$, such that

$$n(T, \eta) = N_c(T) \exp(\eta). \tag{2.7}$$

25

Similarly, the hole concentration can be derived as

$$p(T, \eta') = N_v(T) \exp(\eta') \tag{2.8}$$

where we have defined

$$N_v(T) \equiv 2 \left(\frac{2\pi m_h^* k_b T}{h^2} \right)^{3/2} \quad \text{and} \quad \eta' \equiv \frac{E_v - E_F}{k_b T}.$$

In the intrinsic regime, n equals p because each electron in the conduction band leaves behind a hole in the valence band. Therefore, we can set Eq. (2.7) equal to Eq. (2.8) and find

$$n(T) = p(T) = \sqrt{N_c N_v} \exp\left(-\frac{E_g}{2k_b T} \right) \propto T^{3/2} \exp\left(-\frac{E_g}{2k_b T} \right)$$

where we have replaced $E_c - E_v$ by the bandgap E_g. Consider taking temperature-dependent Hall effect measurements in the intrinsic regime. Then the measured Hall coefficient is given by Eq. (2.3), which includes n, μ_h, and μ_e. In general, the temperature dependence of hole and electron mobilities is affected by carrier scattering due to acoustic phonons, ionized impurities, neutral impurities, or other carriers [43]. At high enough temperatures, acoustic phonon scattering tends to dominate over other mechanisms, and the phonon-limited mobility may be expressed as [43]

$$\mu_L = \mu_{L_0} \left(\frac{T}{T_0} \right)^{-\alpha} \tag{2.9}$$

where $\alpha > 0$ depends on the nature of the carriers and the temperature range. If we assume that both electron and hole mobility follow the same power law temperature dependence, then we see that the temperature dependence of the term in parenthesis in Eq. (2.3) cancels. We are left only with the temperature dependence contained within $n(T)$, such that

$$R_H \propto T^{-3/2} \exp\left(\frac{E_g}{2k_b T} \right). \tag{2.10}$$

Therefore, with the assumptions of parabolic bands and acoustic phonon-limited hole
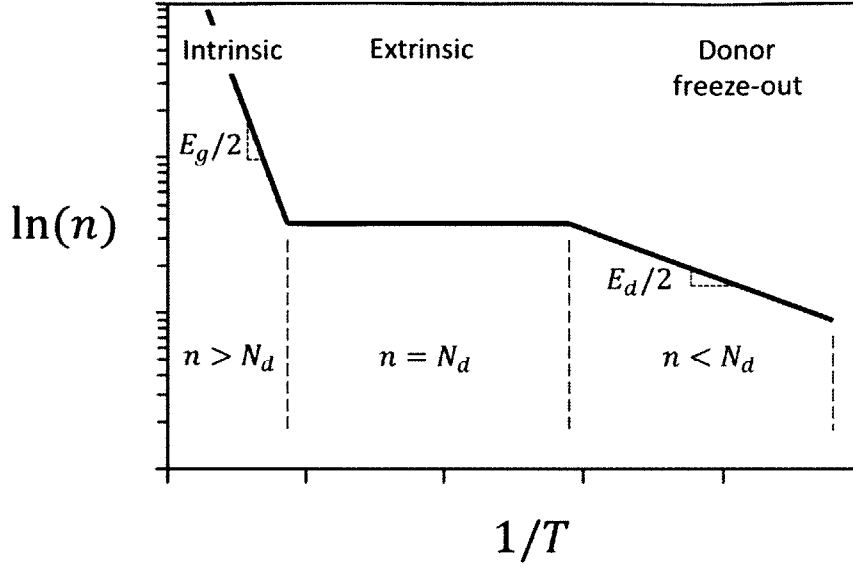
Figure 2-3: Typical form of carrier concentration versus temperature for a semiconductor with a monovalent donor. The intrinsic regime is dominated by valence-conduction band excitations; the extrinsic regime is dominated by ionized donors; and electrons relax back into the donor states in the freeze-out regime. Note that the Arrhenius slope of $E_g/2$ is an approximation valid only when the exponential term in Eq.(2.10) dominates the $T^{3/2}$ term. Adapted from [42].

and electron mobilities, it is possible to measure the bandgap of a material by examining the temperature-dependence of the Hall coefficient in the intrinsic regime. Furthermore, since $\sigma = \mu_{Hall} R_H$, we also find that

$$\sigma \propto T^{\alpha+3/2} \exp\left(-\frac{E_g}{2k_b T}\right).$$ (2.11)

where α is defined in (2.9). The three temperature regimes described above are depicted in Figure 2-3.

2.3 Measuring the intrinsic regime in FeS_2

As mentioned before, care must be taken to operate at temperatures and sulfur partial pressures for which the pyrite FeS_2 phase is most stable. This regime of stability is governed by the phase diagram of pyrite in terms of sulfur partial pressure and temperature. Fortunately, the Fe-S system does not contain any phases which are
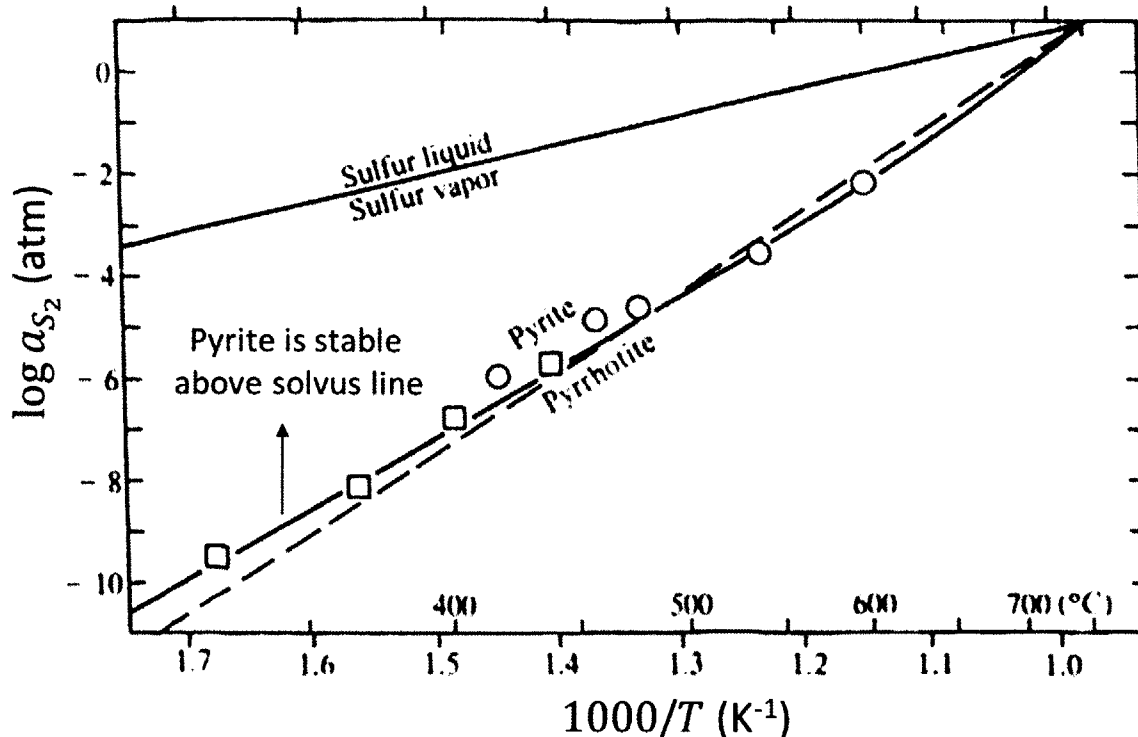
27

Figure 2-4: Phase diagram of sulfur (S_2) partial pressure versus temperature, showing the pyrite-pyrrhotite solvus line. After [45].

more sulfur-rich than FeS_2 [39]. Therefore the regime of stability is bounded only on one side by the pyrite-pyrrhotite solvus line, shown in Figure 2-4. In order to maintain the pyrite phase, we must operate above the pyrite-pyrrhotite solvus line; that is, we must maintain a sulfur partial pressure higher than that of the solvus line at a given temperature.

The equilibrium vapor pressure of sulfur S_2 over solid sulfur has been measured by [44], and for all temperatures shown in Figure 2-4, the equilibrium vapor pressure of sulfur S_2 over solid sulfur is higher than that of the pyrite-pyrrhotite solvus line. Therefore, if we put solid sulfur in a closed system with pyrite, we would expect that the partial pressure of sulfur in the system due to the solid sulfur would be high enough to maintain the pyrite phase. This is the idea which motivated building a custom sulfur chamber for sample measurements, discussed in Section 3.4.2.

Chapter 3

Experimental methods

3.1 Synthesis of single-crystal FeS$_2$

In this work, both natural and synthetic single-crystalline FeS$_2$ were measured. The natural crystals were originally obtained from a Spanish mine, though the exact location is unknown. Several of the natural crystals were crushed to a fine powder with a mortar and pestle for X-ray diffraction (XRD) measurements. No secondary phases were detected by XRD on the representative powder samples.

The natural crystals had unknown concentrations of extrinsic impurities. In order to have better control of impurity concentrations, we also measured synthetically grown single-crystal FeS$_2$, grown by a collaborator using a chemical vapor transport (CVT) process. The process mechanisms are described in detail in [5], but here we list only the methods. First, >99.5% pure Fe powder was mixed with 99.99% pure S powder in a 1:2 stoichiometric ratio. Both powders were obtained from Alfa Aesar. The powder mixture was then sealed under a vacuum in a quartz tube of diameter 1 cm and length 20 cm, along with 0.2 g of FeBr$_3$. The powders were pre-reacted at 600°C for 48 hours, at which point they formed polycrystalline pyrite aggregates. The contents were then removed and placed on one end of a similarly sized quartz tube, which was subsequently sealed. The tube was then placed in a two-zone furnace with a temperature gradient from 700°C at the end containing the polycrystalline powder, to 550 °C at the other end. The tube was left in the furnace for >10 days. The

resulting crystals were either cuboidal or octahedral in shape with linear dimensions of 1-5 mm. Again, phase purity was confirmed by XRD on a representative powder sample.

For both the natural and synthetic crystals, the largest growth faces were identified as (100) by electron back-scattered diffraction in a Zeiss Supra-55 scanning electron microscope.

3.2   Preparation of single crystals for measurement

Prior to optical and electrical measurements, the single crystals were thinned down to a slab of thickness 100-600 μm using mechanical polishing. The two opposing (100) faces were polished to 3 μm roughness by using succesively finer grades of silicon carbide sandpaper, starting with 600 grit and ending with 1200 grit. Polishing was followed by sonication in acetone for five minutes to remove organic contaminants.

Thicknesses of the cleaned crystals were measured using a bench micrometer. The four samples used for electrical measurements (N1, N2, S1, S2) are summarized in Table 3.1. Samples N1 and N2 were natural crystals, and samples S1 and S2 were synthetically grown crystals.

Sample	Crystal type	Thickness (μm)	Measured quantities
S1	Synthetic	528	$\rho(T)$
S2	Synthetic	279	$\rho(T)$, $R_H(T)$
N1	Natural	307	$\rho(T)$
N2	Natural	460	$\rho(T)$, $R_H(T)$

Table 3.1: A total of four samples were used for electrical measurements in a sulfur atmosphere. Resistivity measurements were taken on samples S1 and N1 using the tube furnace setup described in Section 3.4.1, while both resistivity and Hall effect measurements were taken on Samples S2 and N2 using the custom sample chamber described in Section 3.4.2.

3.3   Optical measurements

Optical measurements were performed on both natural and synthetic crystals at room temperature using a Perkin Elmer Lambda 950 UV/Vis/NIR spectrophotometer with

an 8° incident beam. A silver mirror was used to reference specular reflectivity measurements. Absorption coefficient values were calculated using experimental transmission and reflection data, taking into account multiple internal reflections. For a single slab of material, the measured transmissivity T_m and measured reflectivity R_m are related to the actual reflectivity R at the slab-air interface by

$$T_m = \frac{(1-R)^2 \exp^{-\alpha t}}{1 - R^2 \exp^{-2\alpha t}} \quad \text{and} \quad R_m = R(1 + T_m \exp^{-\alpha t})$$

where α and t are the absorption coefficient and thickness of the slab, respectively. The absorption coefficient was found by solving the above equations numerically for α.

Truncation of the presented energy range for each data set was determined by the reliability of the transmission data. At high energies, the transmission intensity falls below the detection limit of the spectrophotometer, and at low enough energies, the transmission intensity cannot be distinguished from the baseline transmission measurement.

3.4   Electrical measurements

3.4.1   Conductivity measurements up to 690 K

Conductivity measurements up to 690 K were performed in a pre-existing two-zone gas-flow tube furnace. The furnace consisted of a quartz tube of inner diameter 47 mm and length 81 cm. The furnace tube ends were sealed with Kalrez o-rings to custom-machined 304 stainless steel endcaps each containing one gas inlet. Each endcap was outfitted with an additional feedthrough for an 1/4 in inner diameter quartz tube which extended into the corrensponding zone of the furnace. K-type thermocouples inserted into these quartz tubes allowed for in-situ temperature measurement. One of the endcaps was outfitted with an electrical feed-through containing four isolated electrical leads. Each zone was heated with coiled nichrome resistive heating elements wrapped around the furnace tube and insulated with quartz wool. Zones were

separated by a 7.5 cm unheated portion, and each zone was 18 cm long.

One significant effort of this thesis was the design and construction of a sample stage that was both resistant to sulfur corrosion and formed ohmic contact with the sample. Because of the assymetric shape of the samples, the Van der Pauw method of measuring resistivity was chosen. The Van der Pauw method does not depend on the geometry of the sample, so long as there are four contacts on the top surface near the edges of the sample [41].

The final sample stage, shown in Figure 3-1, consisted of a square inconel base plate with a counterbored hole at each corner. Electrically insulating washers were fit into the counterbores, and screws were fed through the holes and tightened with an opposing nut. These four screws served as electrical posts on which electrical probes were mounted. Probes were fabricated by spot welding Pt-Ir (90%/10%) wire to inconel cantilevers. The Pt-Ir wire was bent into the shape shown in Figure 3-1a to achieve the desired stiffness.

Samples N1 and S1 were mounted onto an MgO substrate with a water-based high-temperature epoxy (Omegabond 700). After curing, the substrate was placed at the center of the inconcel base plate. Contact to the pyrite surface was made at four points by tightening the cantilevers down on the screw posts with nuts. This formed a reliable mechanical contact between the Pt-Ir wire and pyrite surface. The Pt-Ir/FeS$_2$ electrical contact was found to be ohmic in the voltage range of interest for conductivity measurements.

The sample stage was positioned in the center of the high-temperature zone (Zone 1) as depicted in Figure 3-2. Pt-Ir lead wires connected the sample stage posts to the electrical feedthroughs. ~10 g of 99.999% pure S$_2$ powder, obtained from Alpha Aesar, was placed in a quartz boat in the center of Zone 2, which was kept at 500 K. Argon gas flowing at 10 sccm served as a carrier for the sulfur vapor. The total pressure was measured upstream of Zone 2 at room temperature and kept constant at 25 mTorr. A simplified overview of the setup is shown in Figure 3-2.

The temperature of Zone 1 was allowed to stabilize to within 1°C before each conductivity measurement. A Keithley 4200 sourcemeter was used for current sourcing
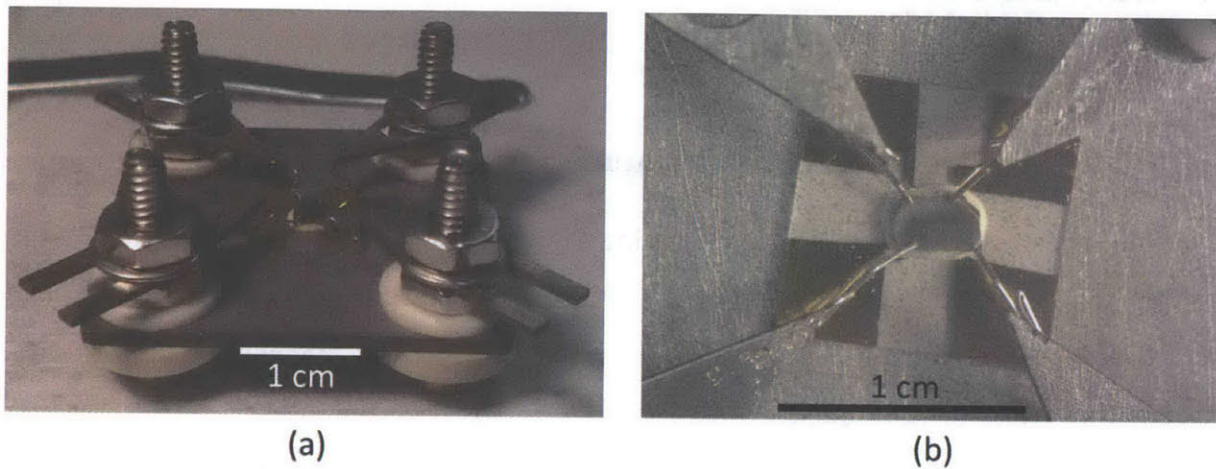
Figure 3-1: (a) Sample stage for resistivity measurements in the tube furnace. (b) Top view of sample probes and sample bonded to the MgO substrate. Note: the four gold contact pads shown surrounding the sample were note used.
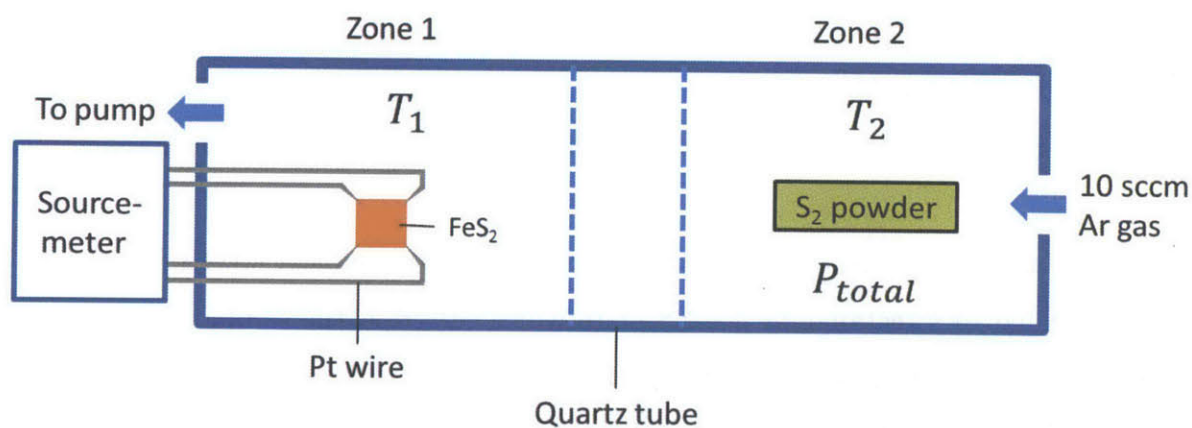

Figure 3-2: Simplified schematic of the tube furnace setup for resistivity measurements. T_1 was varied from 300-690K, T_2 was held constant at 500K, and P_{total} was held constant at 25mTorr. Note that P_{total} was mesaured at room temperature upstream of Zone 2.

($\sim$10mA) and voltage measurement. We observed no sample heating effects. Secondary phases such as FeS were not detected by XRD taken on sacrifical samples under the same operating conditions.

3.4.2 Hall effect measurements up to 600 K

Hall measurements were conducted using a pre-existing closed-cycle helium cryostat capable of temperatures $10 < T < 800$ K. The cryostat assembly fit in between the cores of a Helmholtz coil electromagnet, which provided the magnetic field necessary for Hall effect measurements.

Under its normal mode of operation, the cryostat cold finger is kept under a moderate vacuum ($< 10^{-3}$ torr) in order to thermally isolate the finger from the cryostat walls. However, as explained in Section 2.3, a nonzero sulfur partial pressure over the sample is necessary to maintain the pyrite phase. This requirement called for a custom sample chamber which could fit onto the cold finger of the cryostat and keep the necessary sulfur partial pressure over the sample while keeping the sulfur gas isolated from the vacuum of the cryostat.

The design and construction of such a sample chamber was a major effort during this thesis. The final sample chamber consisted of a flanged sample stage assembly, electrical feedthroughs, a metal gasket seal, and a chamber tube, shown schematically in Figure 3-3. Appendix A contains dimensioned drawings of the final sample chamber.

The flanged stage assembly was composed of a 304 stainless steel (SS) conflat flange welded to a rectangular 304 SS plate which served as the sample stage. Electrical contact to a centrally mounted pyrite sample was made in a similar fashion to that of the sample stage discussed in Section 3.4.1. The main difference was that the components were smaller due to the size constraints of the cryostat. Four 304 SS screws, electrically isolated from the sample stage plate by ceramic washers, served as mechanical posts on which electrical probes were mounted. The electrical probes were made with 304 SS washers spot welded to Pt-Ir wires bent into the desired shape. The pyrite sample rested on a ceramic disc for electrical isolation. Since the sample
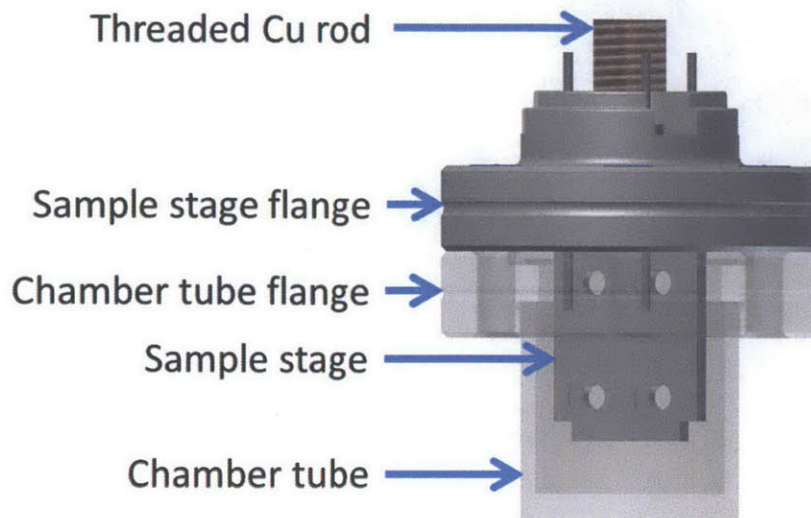
34

Figure 3-3: Sample chamber assembly. All components except the Cu threaded rod were 304 stainless steel.

stage would be mounted into the cryostat vertically, the electrical probes also served to mechanically clamp the sample to the stage. The sample stage assembly is shown in Figure 3-4.

Four commercially available electrical feedthroughs, each consisting of 304 SS leads Cu-brazed into an hollow ceramic cylinder, were welded onto the conflat flange to form a leak-tight seal. The leads on the inside of the chamber were clipped, bent, and spot-welded to the four electrical posts using Pt-Ir wire.

~1 g of 99.999% pure S_2 powder was placed inside the flanged tube. The chamber tube was then sealed to the flanged sample holder in a glovebox with N_2 atmosphere (< 5 ppm O_2) using a Ni gasket. The sample chamber assembly was connected to the cold finger of the cryostat via a threaded Cu rod, which formed a good thermal contact.

Standard techniques [41] were used to measure the conductivity and Hall effect. Signal multiplexing allowed correction of standard errors by collecting redundant measurements of the Hall voltage. The sample chamber was immersed in a magnetic field of ~ 0.7 T, and data were collected for both positive and negative fields. Currents were kept at the lowest possible to generate a Hall voltage of ~ 10 μV. We observed no self-heating effects.
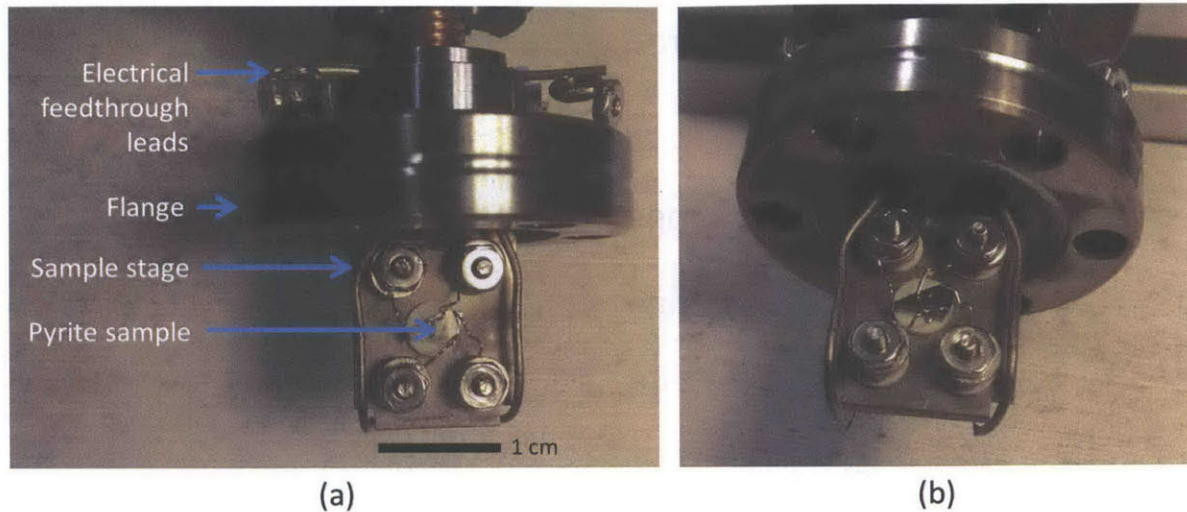
Figure 3-4: Flanged sample stage assembly. (a) Side view showing the sample holder face-on. Not labeled are the four electrical posts with electrical probes contacting the sample. (b) Angled view which shows the groove for the Ni gasket more clearly.

The Hall mobility was calculated using

$$\mu_{Hall} = R_H \sigma$$

where R_H is the measured Hall coefficient and σ is the measured conductivity.

We began measurements at low temperatures and proceeded with progressively higher temperatures. Under operating conditions, it was found that the 304 SS components and Ni gasket formed a self-limiting sulfide layer. However, the sulfur consumed during this initial sulfurization was found to be negligible. The electrical feedthroughs did allow a measurable sulfur leak via diffusion through the Cu brazes, but the leak rate was found to be small enough to maintain the required sulfur partial pressure above the sample over the duration of the measurement. Secondary phases such as FeS were not detected by XRD taken on sacrifical samples under the same operating conditions.

Conductivity and Hall effect measurements were taken on samples S2 and N2 up to 500 K, but only on N2 up to 710 K. Data beyond 710 K was unreliable due to anomolous electrical noise.

Chapter 4

Results

4.1 Optical measurements

The measured optical absorption coefficients are shown in Figure 4-1. The varying energy ranges across data sets were due to the varying thicknesses of the corresponding crystals, which resulted in varying transmission cutoff energies. The lower plot shows the same data on semilog axes.

4.2 Electrical measurements

4.2.1 Conductivity measurements

The conductivity of samples S1, S2, N1, and N2 are shown in Figure 4-2. For synthetic crystals, we see a monotonic increase in conductivity with temperature. However, the conductivity temperature dependence of natural crystals varies widely. For sample N1, the conductivity monotonically decreases with increasing temperature from room temperature to 510 K, while sample N2 monotonically increases in the same range.

4.2.2 Hall effect measurements

The Hall coefficients measured using the custom sample chamber are shown in Figure 4-3. All samples were found to be n-type semiconductors, indicated by a negative
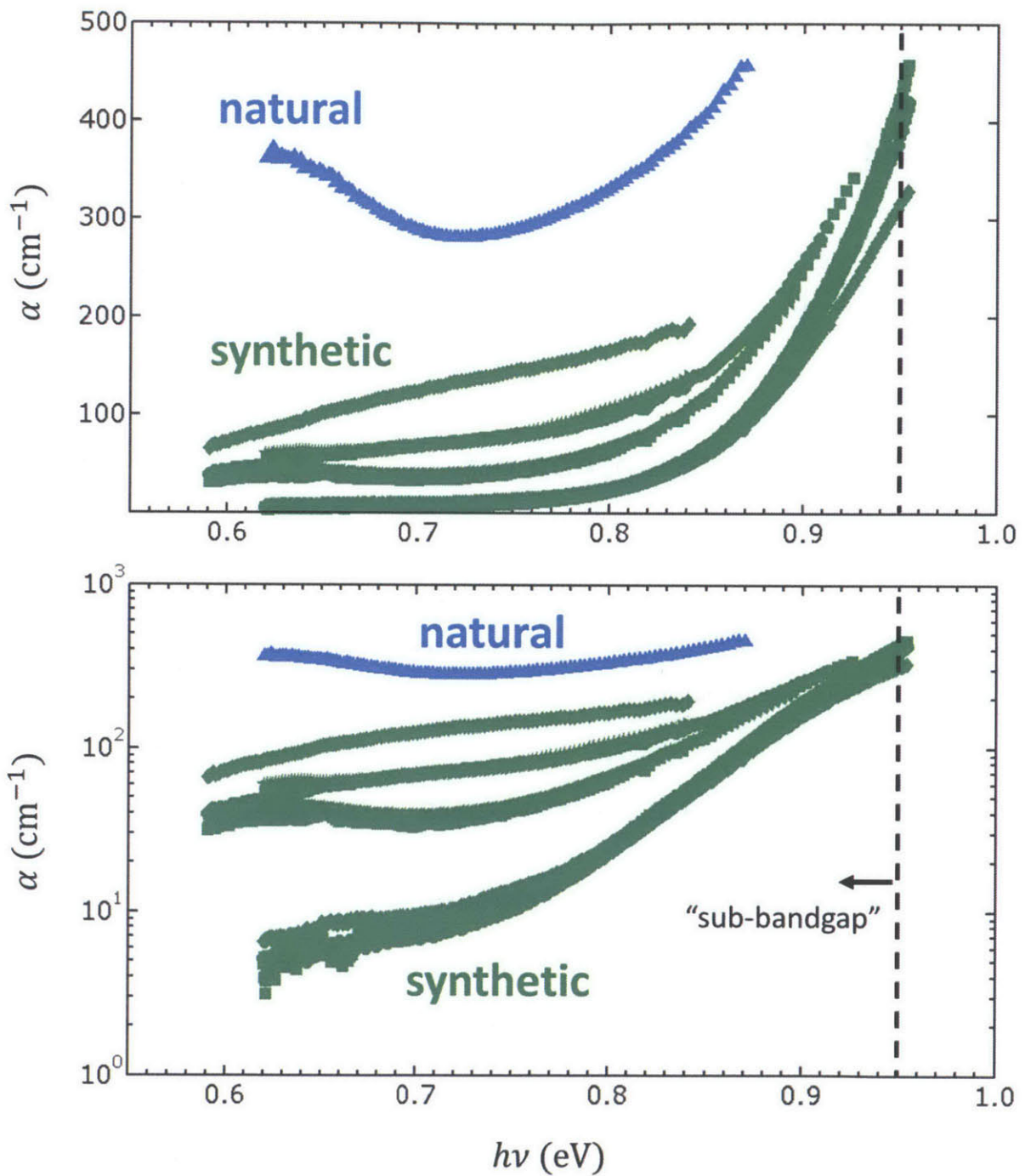
Figure 4-1: Measured absorption coefficient of single-crystalline samples. Natural crystal data shown in blue; synthetic crystal data shown in green.
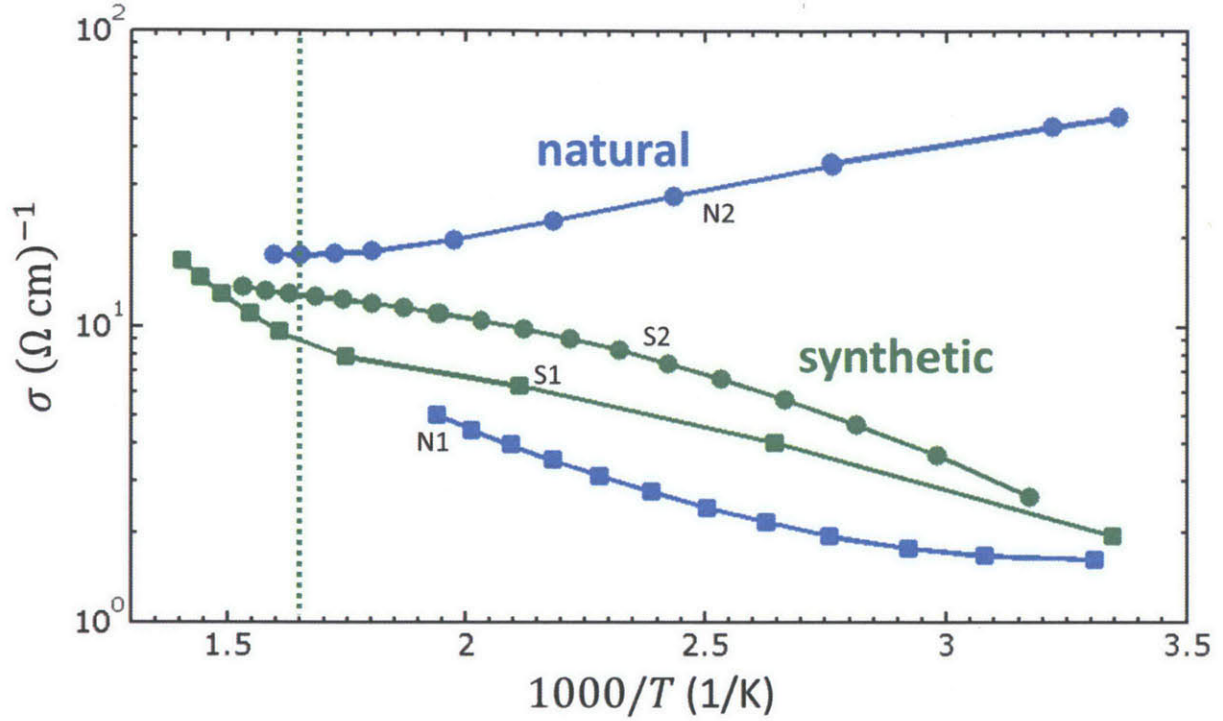
Figure 4-2: Conductivity temperature dependence. Green data points indicate synthetically grown crystals; blue points indicate natural single-crystals. Square data points indicate measurements using the tube furnace described in Section 3.4.1, and circular data points indicate measurements using the custom sample chamber described in Section 3.4.2.

Hall coefficient.

Sample N2 shows a relatively constant Hall coefficient up to ~ 540 K, at which point the Hall coefficient begins decreasing. This change in behavior is consistent with the corresponding conductivity data. The Hall coefficient for sample S2 shows no change in slope.

Figure 4-4 shows the Hall mobility calculated by Eq. (2.4). We observe similar Hall mobilities among the natural and synthetic crystals, with similar temperature dependencies. The red line in Figure 4-4 indicates a Hall mobility following the power law in Eq. (2.9) with $\alpha = 2.0$.
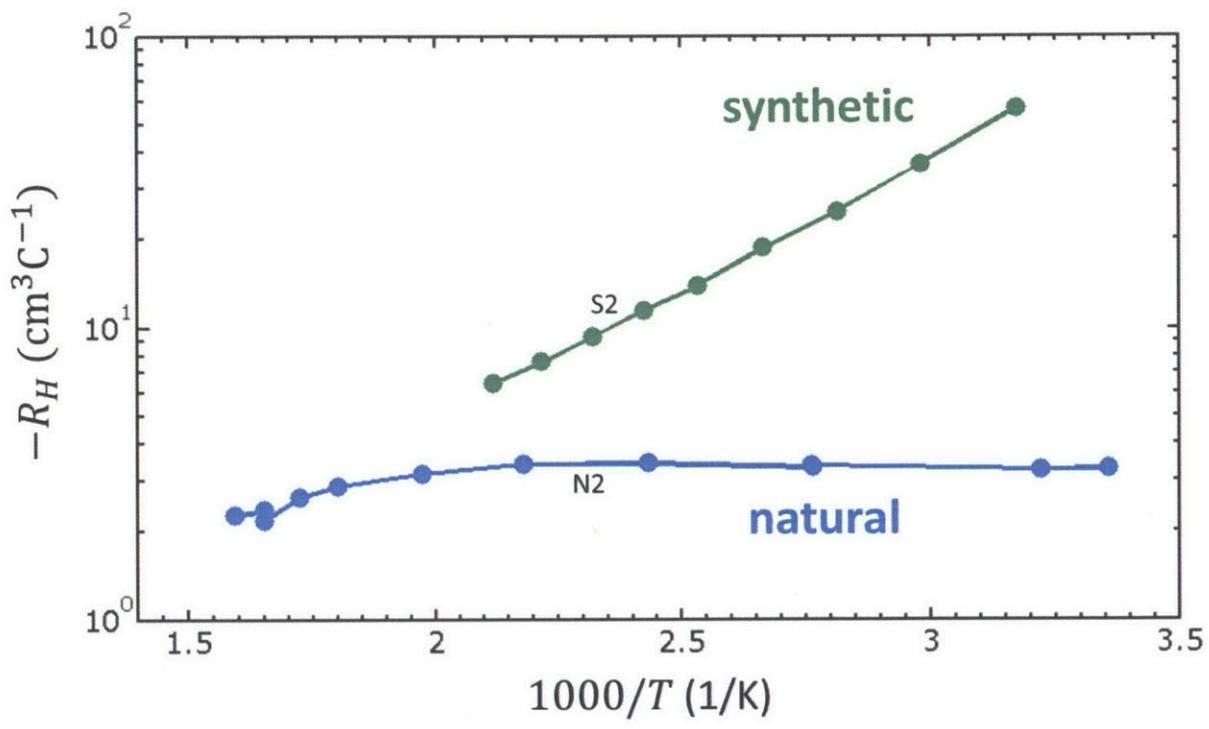
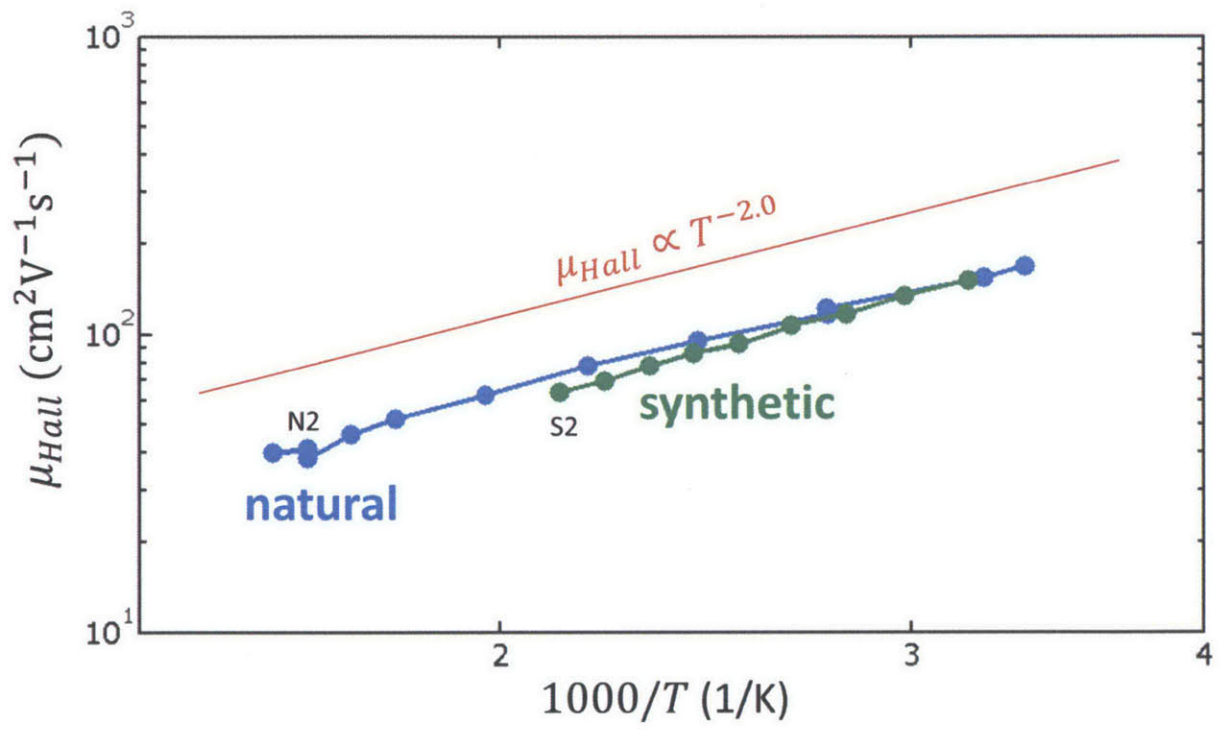Figure 4-3: Hall coefficient measured using the sample chamber up to 600 K.

Figure 4-4: Hall mobility measured using the sample chamber up to 600 K.

THIS PAGE INTENTIONALLY LEFT BLANK

Chapter 5

Discussion

5.1   Optical measurements

From Figure 4-1, we see that the natural crystal exhibits a higher degree of sub-bandgap absorption than the synthetic crystals. This could be attributed to a higher defect concentration in the natural crystal. Certain defects may enhance the sub-bandgap absorption through excitation of the defect states. We have not attempted to measure defect concentration (e.g., extrinsic impurity concentration) in our samples, so we cannot say with certainty that this is the cause of the discrepancy between the natural and synthetic crystals.

Among the synthetic crystals, the absorption coefficient varies by more than one order of magnitude in the 0.6-0.8 eV range. Above 0.8 eV, the absorption coefficient seems to converge across all crystals. This may be due to the decreasing effect of defect absorption at higher photon energies, as band-to-band transitions begin to dominate near the bandgap energy.

We compare our measured absorption coefficient to literature values in Figure 5-1. The literature values presented were all taken on single-crystals, though the plot does not distinguish between natural and synthetically grown crystals in the literature. The large spread among the literature values and our data, especially in the sub-bandgap range, may be due to a number of causes.

First, none of the literature values are obtained using both transmission and re-
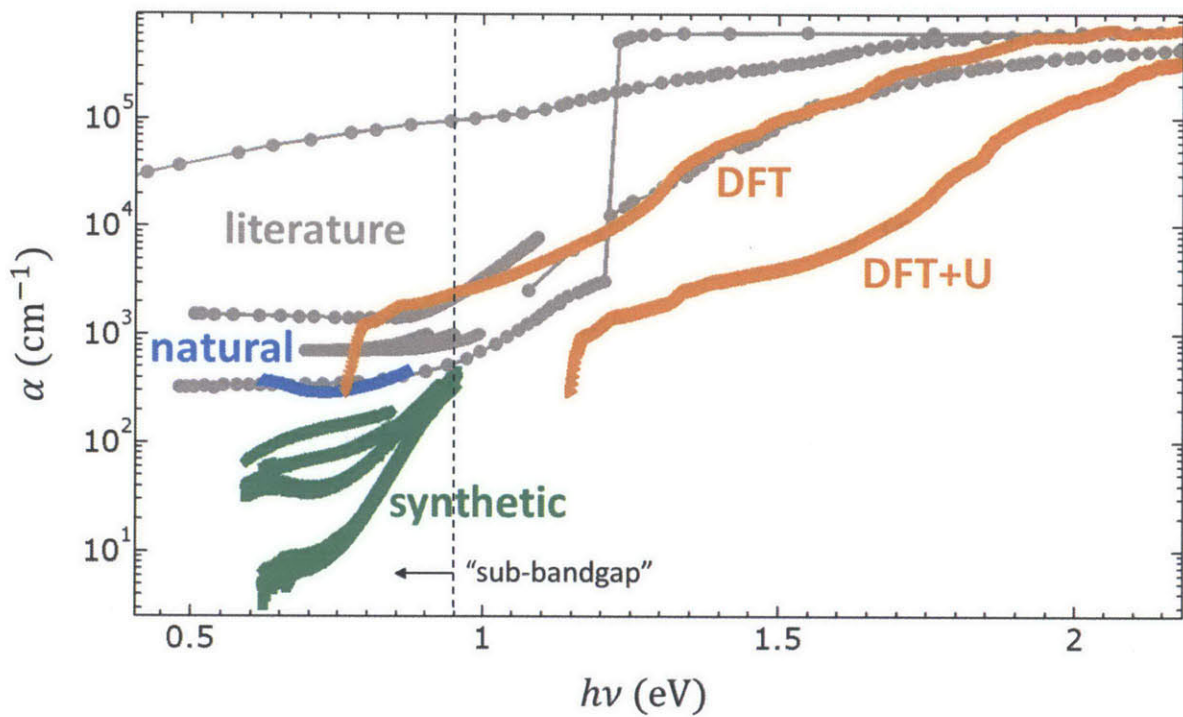
Figure 5-1: Same data as in Figure 4-1 overlayed with literature values of absorption coefficient for single-crystalline pyrite from references [19, 20, 24, 26, 27, 46] (shown in gray) and theoretical values calculated by DFT from [8].

flection data. In two of the studies [24, 26], only transmission was measured. The absorption coefficient was obtained by arguing that the reflectivity does not vary appreciably in the photon energy range of interest. In this case, the absorption coefficient can be calculated without knowledge of the reflectivity, given transmission data on two crystals of different thicknesses. However, it is important to note that this argument is based on reflectivity data taken on other pyrite crystals in the literature. Considering the large variation among literature absorption data, a proper absorption coefficient measurement would require both transmission and reflection measurements on the same crystal.

In the remaining four studies shown in Figure 5-1, only reflection was measured. The authors used the well-known Kramers-Krönig transformation [47] to calculate the absorption coefficient from reflection data alone. The issue with this technique is that strictly speaking, a Kramers-Krönig transform requires computing an integral involving reflectivity over all photon wavelengths, from 0 to ∞. This of course is not experimentally possible, so approximations are used in conjunction with the experimental reflection data to obtain the absorption coefficient. Often, these approximations are unfounded [47], and in the specific cases of [20], [27], [46], and [19], it is at best unclear which approximations are used.

In addition to questionable measurement and analysis techniques, the large spread in the literature values may also be due to a large variance in defect concentration in the samples. Although all samples in the literature were confirmed to be phase-pure, the extrinsic impurity concentrations in the samples were not measured. As suggested above, certain extrinsic impurities may enhance the sub-bandgap absorption through excitation of mid-gap impurity states. Given the relatively large spread in the absorption coefficients of crystals even within this work, as a next step we would like to measure the impurity concentrations in each sample and note how absorption coefficient varies with impurity concentration.

Although our synthetic samples exhibited the least sub-bandgap absorption compared to literature values, the observed sub-gap absorption is non-negligible. We still cannot rule out absorption through mid-gap defect states as a partial cause of the

sub-bandgap absorption in the synthetic crystals, as we have not measured the relevant defect concentrations. However, the data does not disagree with the hypothesis that the currently accepted bandgap of single-crystalline pyrite, 0.95 eV, is an overestimation. Attempts to extract the optical bandgap from our absorption data yielded poor fits because of insufficient absorption data at the high-end range of photon energies. For the purpose of extracting a bandgap, we rely on electrical measurements, discussed in Section 5.2.2.

5.2 Electrical measurements

5.2.1 Conductivity measurements

The large disparity in conductivity of samples N1 and N2 seen in Figure 4-2 is consistent with the spread in the literature [25, 35–38]. The spread may be due to a difference in extrinsic impurity concentration, carrier concentration, or both. Certain impurities such as bromine have been shown to act as donors in pyrite [32], and there are certainly correlations between certain impurities and electrical properties [28]. Again, as a next step we would like to measure the impurity concentrations in our samples and note how the electrical properties vary with impurity concentration.

The synthetic samples exhibit a smaller spread in conductivities, which may be due to a smaller variance in impurity concentration than in the natural samples, as we would expect. The magnitude of the synthetic crystal conductivities is not outside the range of literature values [22, 25, 28–38], although they do fall on the lower end of the range quoted in literature.

As with Hall coefficient, we expect a change in slope of the conductivity at the onset of the intrinsic regime. For samples S2, N1, and N2, no sharp change in slope was observed with increasing temperature, suggesting that the intrinsic regime was not reached. However, for sample S1, such a change in slope was observed at ∼600 K, indicated by the dotted line in Figure 4-2. The data for sample S1 for $T > 600$ K may thus be attributed to the onset of the intrinsic regime.

5.2.2 Estimating the bandgap

Ideally, we would extract the bandgap by fitting the temperature-dependent Hall coefficient data in the intrinsic regime to Eq. (2.10). The first step is to identify the intrinsic regime for each sample, marked by a sharp change in slope of R_H similar to that depicted in Figure 2-3. At low temperatures, we expect a relatively shallow Arrhenius slope due to freeze-out of donors; at intermediate temperatures, we expect a near-zero Arrhenius slope due to the complete ionization of donors; and at high temperatures, we expect a significant change in Arrhenius slope as band-to-band transitions begin to dominate.

Examining Figure 4-3, we identify at least one regime for each of the samples. For sample S2, R_H decreases with a constant Arrhenius slope as temperature increases, consistent with freeze-out regime behavior. Unfortunately, we were unable to obtain reliable Hall effect data at higher temperatures due to anomalous electrical noise in our system.

For sample N2, R_H from room temperature up to $\sim$ 520 K remains nearly constant, consistent with extrinsic regime bahavior. That the synthetic sample exhibits freeze-out behavior while the natural sample exhibits extrinsic-regime behavior suggests that the donor activation energy in the natural sample is less than that in the synthetic sample. That is, the dominant donor species in the natural crystal is different from that of the synthetic sample.

The change in slope of R_H at $\sim$ 520 K for sample N2 indicates the onset of the intrinsic regime. However, because the Hall coefficient varies by only a factor of $\sim$ 50% in this regime, extracting a bandgap from the Arrhenius slope may be a severe underestimate. Higher temperature data is needed such that the Hall coefficient spans at least one order of magnitude before one can reliably fit the data to Eq. (2.10).

Despite the lack of high-temperature R_H data, one may still estimate a bandgap by examining the Hall mobility temperature dependence in Figure 4-4. For both natural and synthetic samples, the Hall mobilities decrease with a distinct Arrhenius slope as temperature increases. Recognizing that this behavior is characteristic of

47

phonon-limited mobility, we fit the data according to Eq. (2.9) and find $\mu \propto T^{-2.0}$ and $\mu \propto T^{-2.2}$ dependencies for sample N2 and S2, respectively (see Appendix B for graphical fits). That the natural and synthetic crystals exhibit similar temperature dependencies despite having widely different carrier concentrations is further evidence of a mobility-limiting mechanism such as acoustic phonon scattering which is independent of carrier concentration.

If we assume that this mobility dependence holds for higher temperatures, and if we assume that the slope of sample S1 conductivity for $T >\sim 600$ K is representative of the intrinsic regime, then we may roughly estimate the bandgap using Eq. (2.11). The high temperature conductivity data ($620 < T < 710$ K) were fitted according to Eq. (2.11) for the two different values of α (2.0 and 2.2) found from mobility data. The fitted bandgaps are $E_g(T_{intrinsic}) = 0.53$ eV and $E_g(T_{intrinsic}) = 0.55$ eV for $\alpha = 2.0$ and $\alpha = 2.2$, respectively. To find the bandgap at room temperature, it is necessary to take into account the temperature-dependence of the bandgap due to lattice expansion and electron-phonon interaction. For many semiconductors including pyrite FeS_2, the variation of the bandgap with temperature has been shown to obey the semi-empirical relation [48]

$$E_g(T) = E_g(0) - \frac{(2.25 \times 10^{-5}\theta_D - 4.275 \times 10^{-3})}{5(T + 5\theta_D - 1135)}T^2, \qquad (5.1)$$

where $\theta_D = 610$ K and $E_g(0)$ represents the bandgap at 0 K. Using Eq.(5.1) in conjunction with our estimates of $E_g(T_{intrinsic})$, we find that the bandgap at room temperature is $E_g(300\,\text{K}) = 0.78 \pm 0.04$ eV for $\alpha = 2.0$, and $E_g(300\,\text{K}) = 0.80 \pm 0.04$ eV for $\alpha = 2.2$. The error bars indicate the range of the calculation from $T_{intrinsic} = 620$ K to $T_{intrinsic} = 710$ K, which was found to be larger than the experimental error. Thus, the best estimate based on our dataset for the room temperature bandgap of pyrite is $E_g = 0.79 \pm 0.05$ eV.

There are several caveats to this bandgap estimate. First, as mentioned in Section 5.2, we cannot be confident that the fitted slope to conductivity is representative of the entire instrinsic regime. As with Hall effect data, higher temperature data is

needed such that the conductivity spans at least one order of magnitude before one can fit the data to Eq. (2.11) with high confidence. Second, the bandgap estimate relies on the extrapolation of mobility to higher temperatures based on the semi-empirical relation $\mu \propto T^{-\alpha}$. Although this extrapolation may be partially justified by recognizing that the dominant mechanism is acoustic-phonon scattering, we would like to have high-temperature mobility data (or equivalently, high-temperature Hall coefficient data) to support this claim. Third, we have assumed that the mobility extrapolation for samples S2 and N2 holds for sample S1 for which conductivity measurements were taken. Ideally, we would like to have mobility and conductivity data on identical samples. However, given that sample S2 and S1 were from the same batch of synthetically grown crystals, we do not expect them to have significantly different electrical properties. Lastly, we have taken electrical data on only two samples: one synthetic and one natural. A larger sample size would greatly increase our certainty in the bandgap measurement.

Keeping the above considerations in mind, our results fall in the lower range of literature values reported for the electrical bandgap of pyrite (see Table 1.2), closest to the 0.77 eV estimate of Horita *et al.* [37]. However, the bandgap measured by Horita *et al.* was measured on natural crystals, with uncontrolled impurity concentrations. Considering only synthetic crystal studies, our estimate of the bandgap is at least 0.11 eV lower than literature values for the electrical bandgap of pyrite [22].

A pyrite bandgap significantly less than the widely quoted literature value of 0.95 eV would have several implications. First, a lower fundamental bangap is consistent with the anomalous sub-bandgap optical absorption observed in single-crystalline pyrite. In the literature, sub-bandgap optical absorption has generally been attributed to defect absorption or disorder in the crystal [19, 20, 24–26], and the sub-bandgap absorption was substracted before fitting the data to extract a bandgap. However, a low-intensity conduction band tail which reduces the fundamental bandgap to as low as 0.5 eV would produce a similar sub-bandgap absorption tail, as shown by Lazić *et al.* [8].

From a photovoltaic device perspective, a pyrite bandgap less than 0.95 eV may

also partially explain the low V_{OC} typical of pyrite solar cell devices. Assuming our estimate of $E_g = 0.79$, the theoretical maximum V_{OC} for a pyrite solar cell would be reduced to ~400 mV, ~100 mV lower than previously thought [5]. This alone does not explain the still-low V_{OC} of 187 mV measured for the record-efficiency device [5], but may account for a non-trivial fraction of the perceived V_{OC} deficit. The remainder of the defficiency may be due to a lowering of the bandgap at the surface of pyrite, which is supported by recent theoretical and experimental work [8, 18].

Chapter 6

Conclusion

In this work, the origin of sub-bandgap absorption in pyrite FeS_2 was investigated through optical and electrical measurements on single-crystals. Both natural and synthetic single-crystals exhibited non-trivial magnitudes of sub-bandgap absorption, which may partially be due to a lower FeS_2 bandgap than previously thought. To test this hypothesis, temperature-dependent electrical transport properties were measured in the intrinsic and near-intrinsic regimes of pyrite under a sulfur atmosphere. The sulfur atmosphere successfully maintained the pyrite phase during the measurements. Due to experimental limitations, we were unable to obtain sufficient Hall effect data in the intrinsic regime. However, using intrinsic-regime conductivity data in conjunction with extrapolation of Hall mobility into the intrinsic regime, the extracted bandgap was 0.79 ± 0.05 eV. In light of our current results and the possible implications of a pyrite bandgap less than the 0.95 eV widely quoted in the literature, we believe a continued investigation of the pyrite bandgap is warranted. In particular, a thorough study of the effects of impurity concentration, higher-temperature Hall effect data in sulfur atmosphere, and a larger sample size are necessary to achieve greater certainty in the fundamental bandgap of pyrite.

THIS PAGE INTENTIONALLY LEFT BLANK
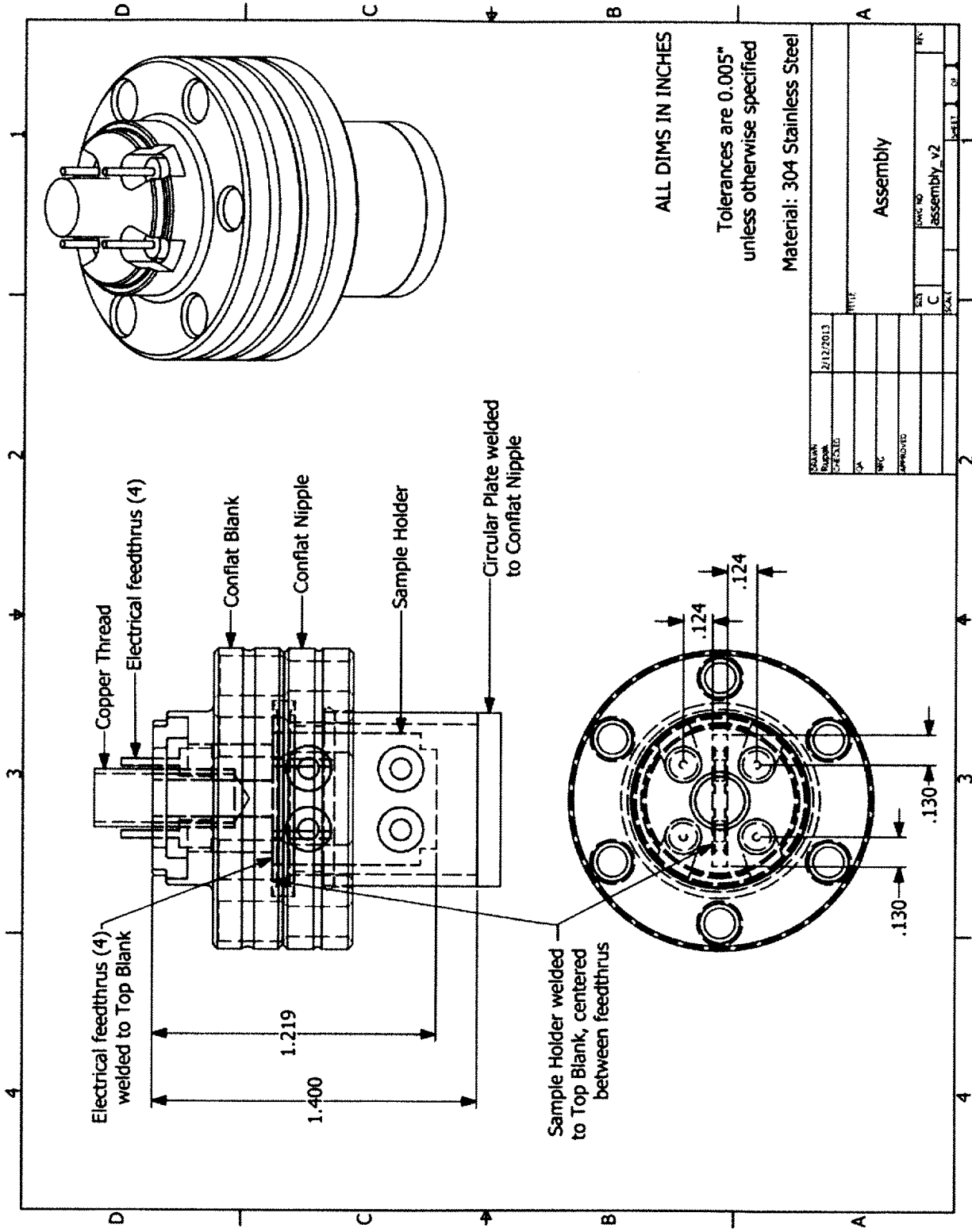
Appendix A

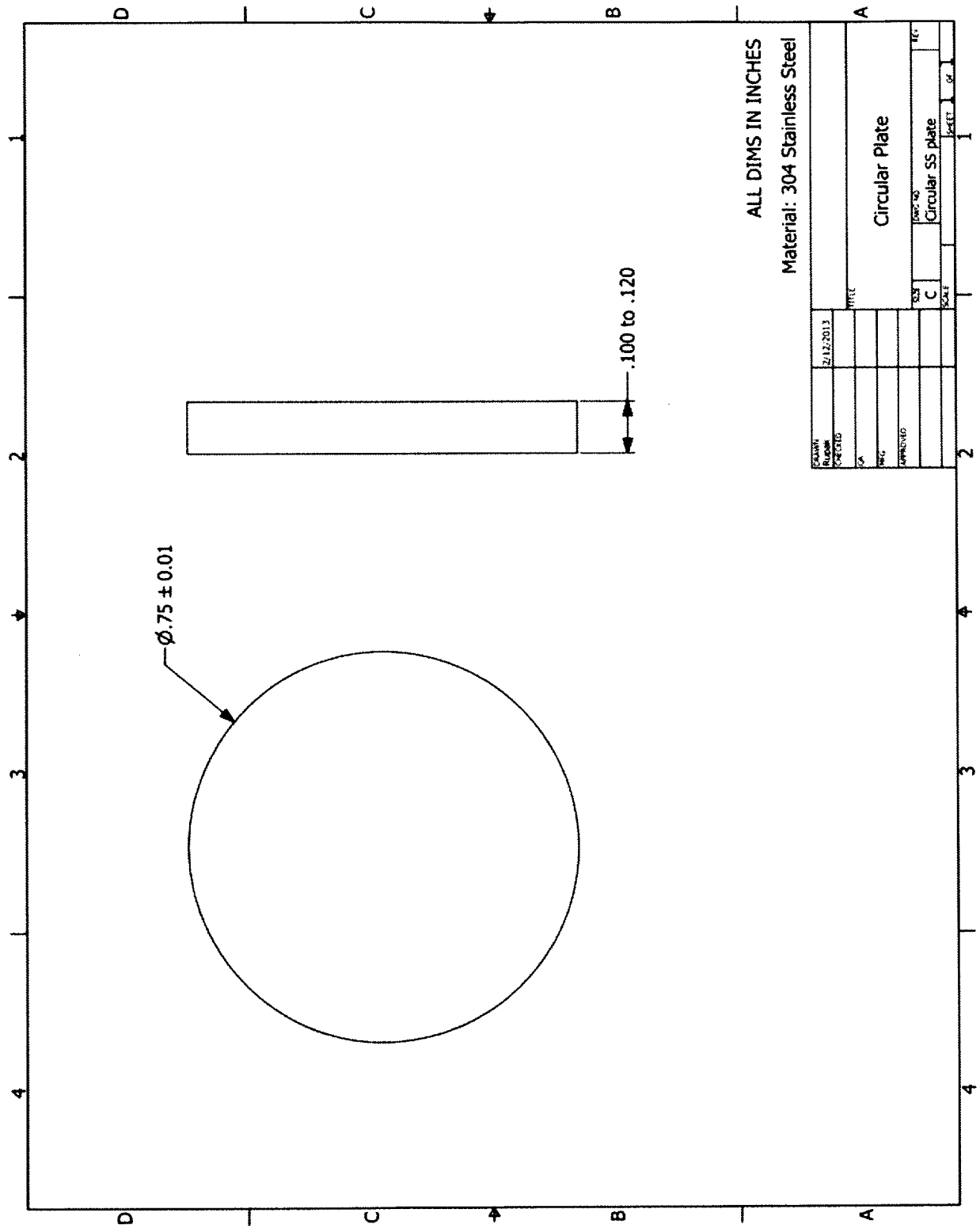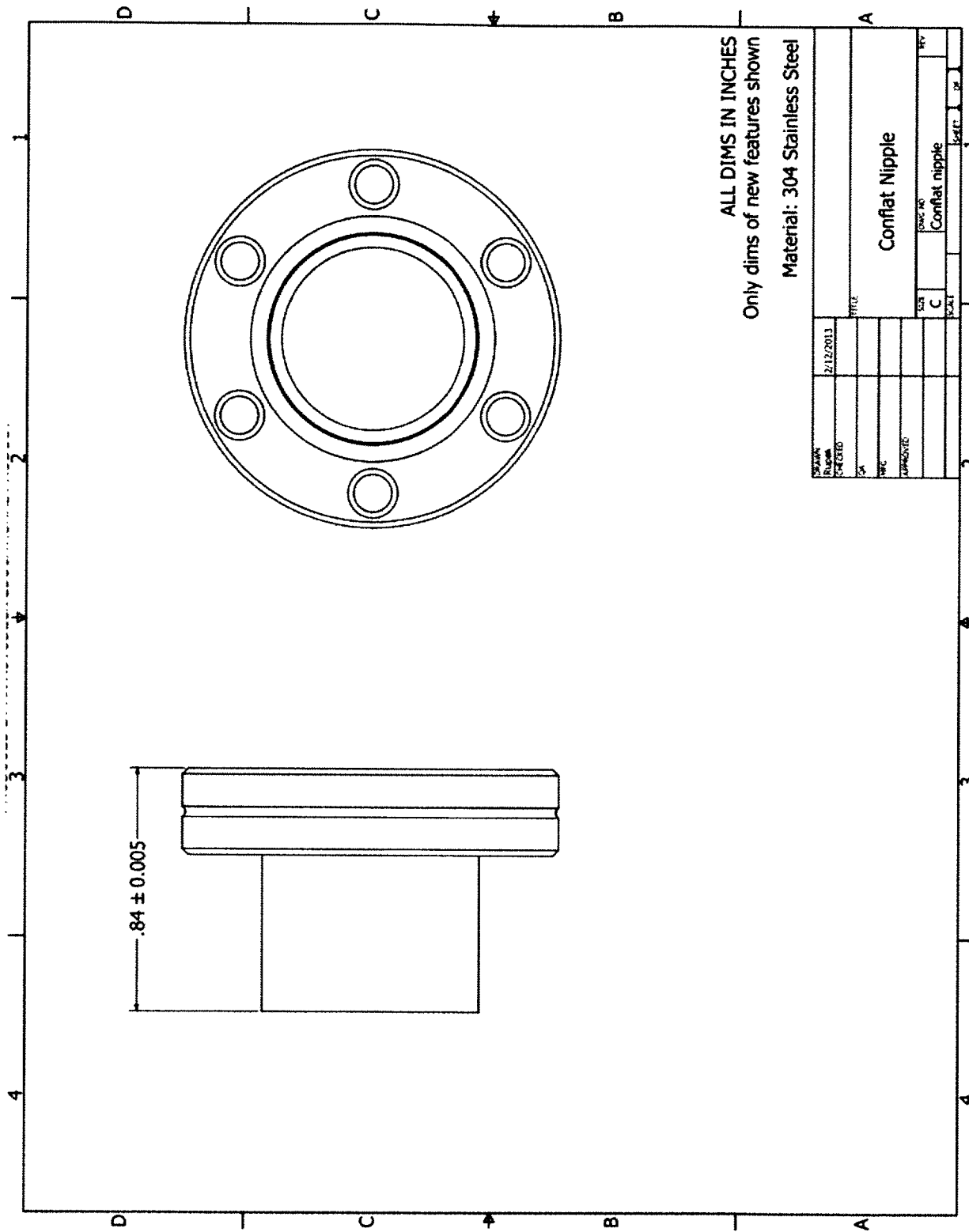# Drawings of sample chamber parts

Figure A-1: Sample chamber assembly.

Figure A-2: Circular plate welded onto bottom of sample chamber.

The drawing contains the following labels:

ALL DIMS IN INCHES
Only dims of new features shown

Material: 304 Stainless Steel

Conflat Nipple

Conflat nipple

2/12/2013

.84 ± 0.005

Figure A-3: Sample chamber tube.

ALL DIMS IN INCHES

Material: Copper

Ø.250

1/4-28 UNF

.600 ± 0.005

Copper Thread

Copper thread

2/12/2013

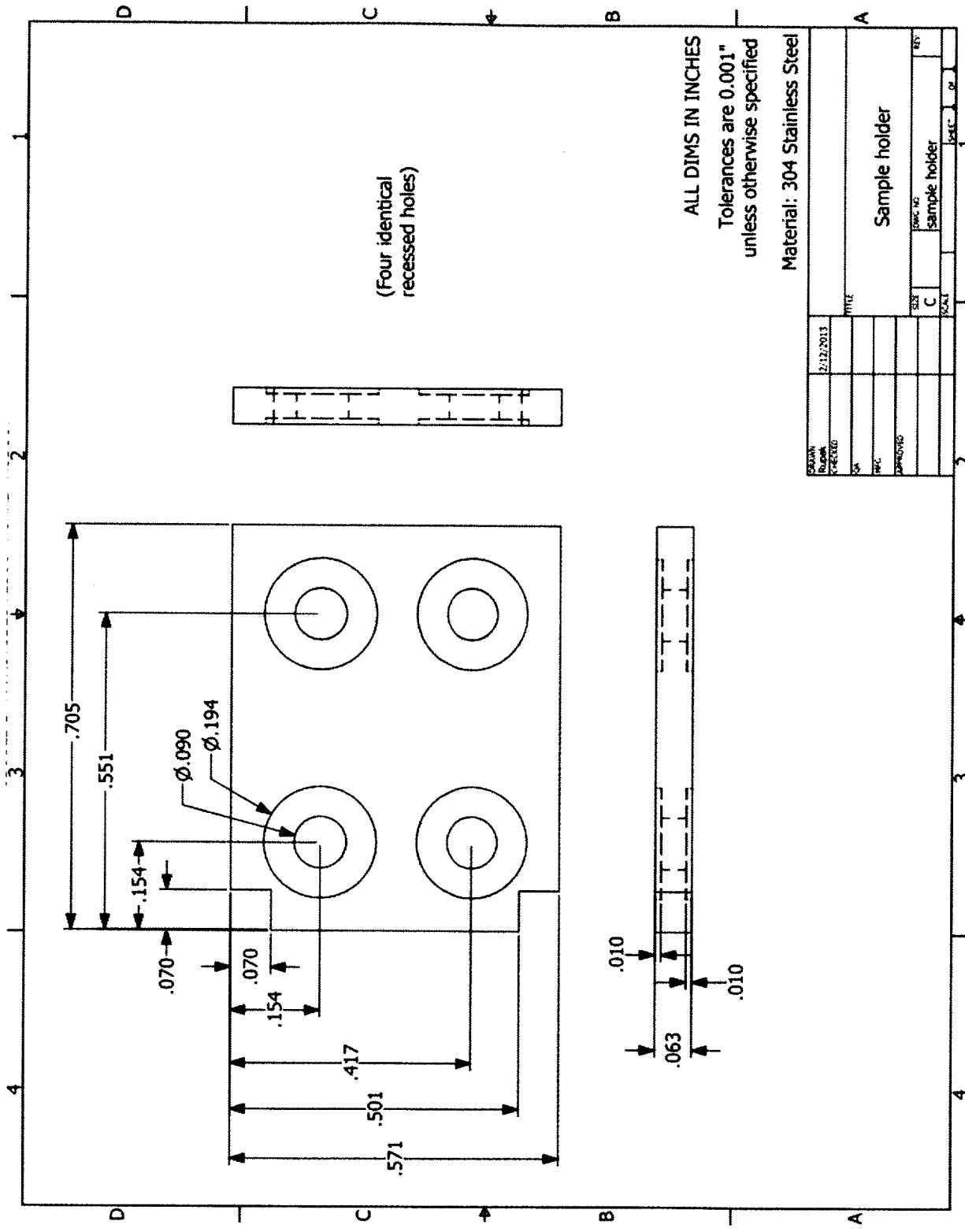Figure A-4: Copper thread connecting sample chamber to cryostat cold finger.
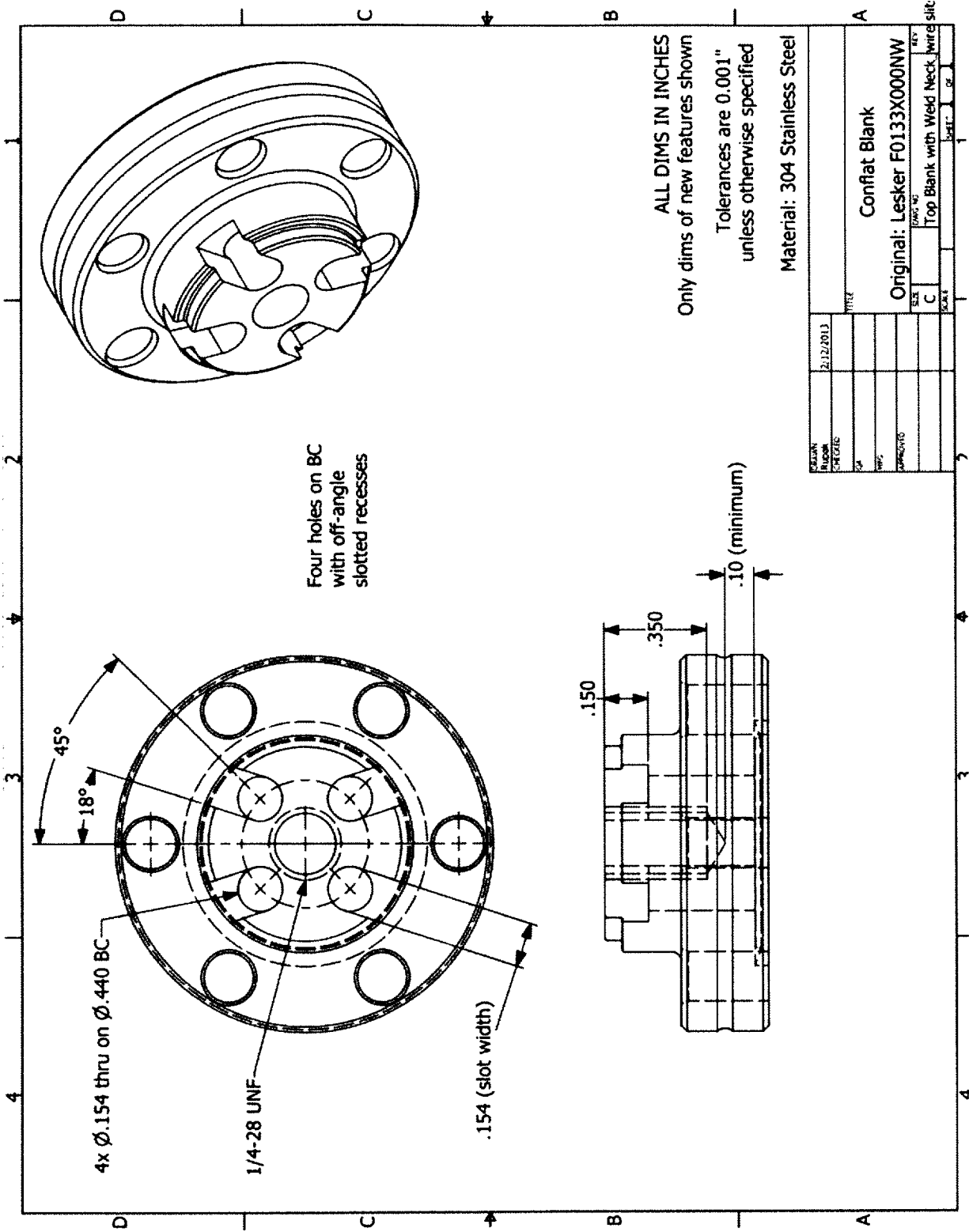
Figure A-5: Sample stage plate.

Figure A-6: Sample stage flange.

THIS PAGE INTENTIONALLY LEFT BLANK

Appendix B

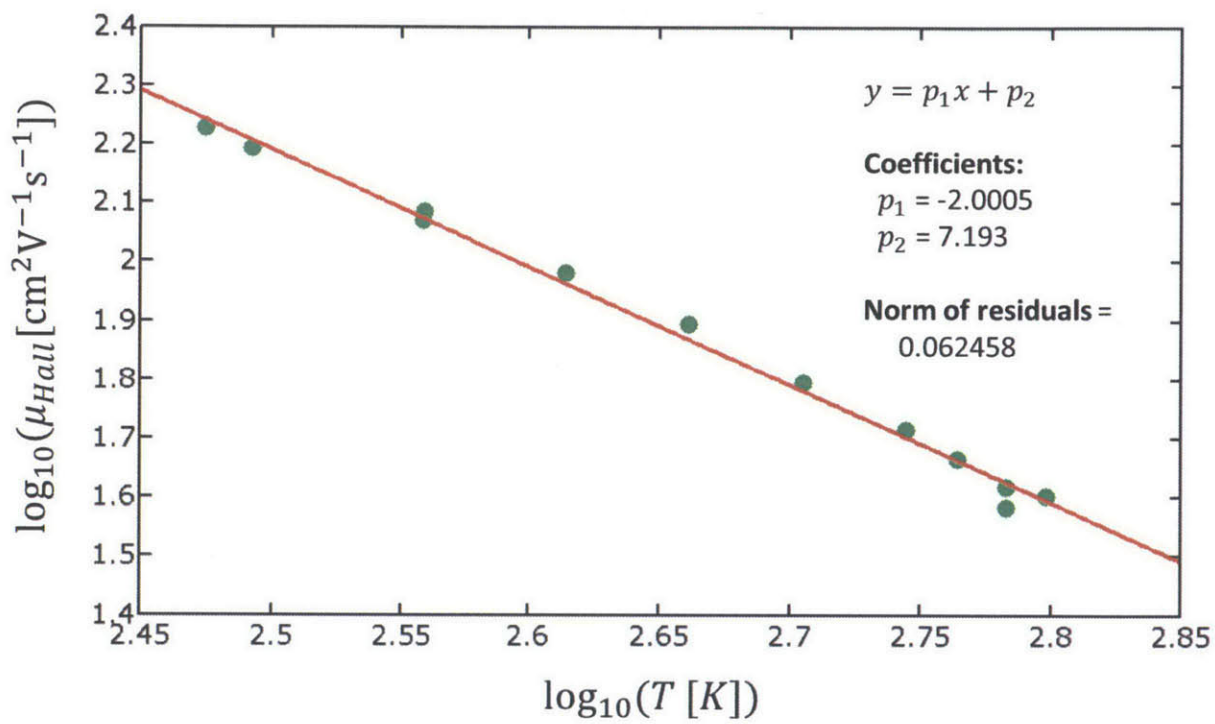# Hall mobility and conductivity fits

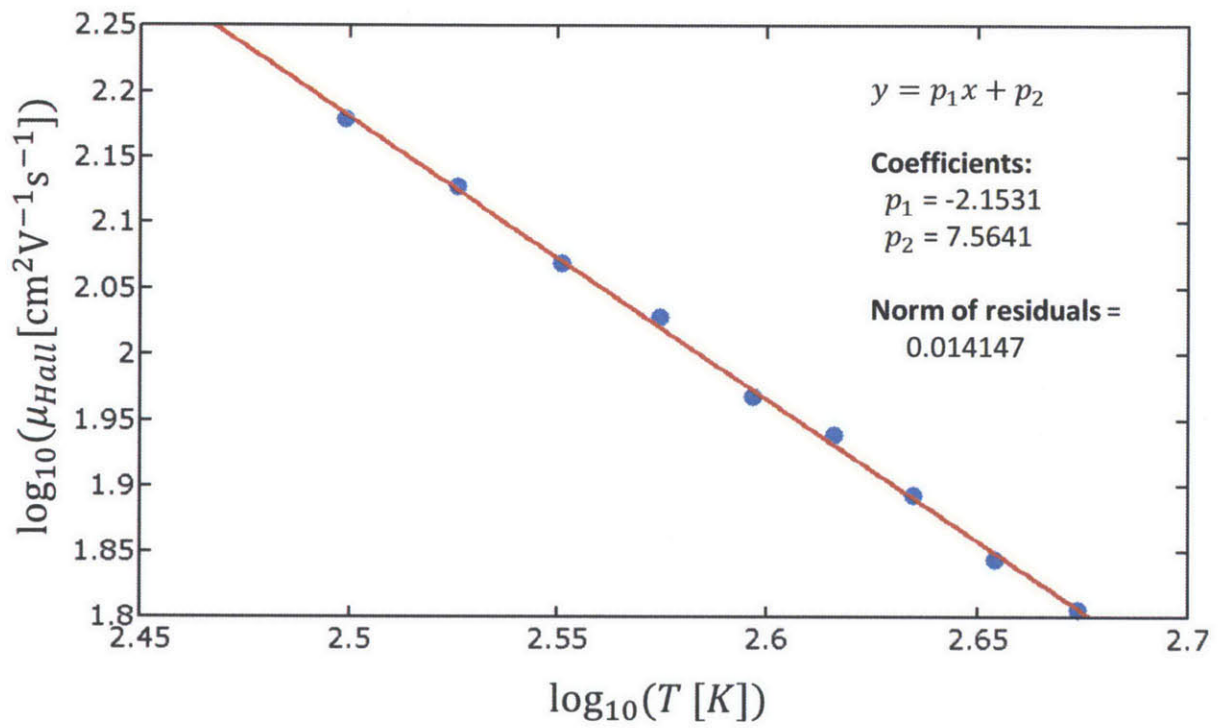Figure B-1: $\mu_{Hall} \propto T^{-\alpha}$ fit for sample S2.

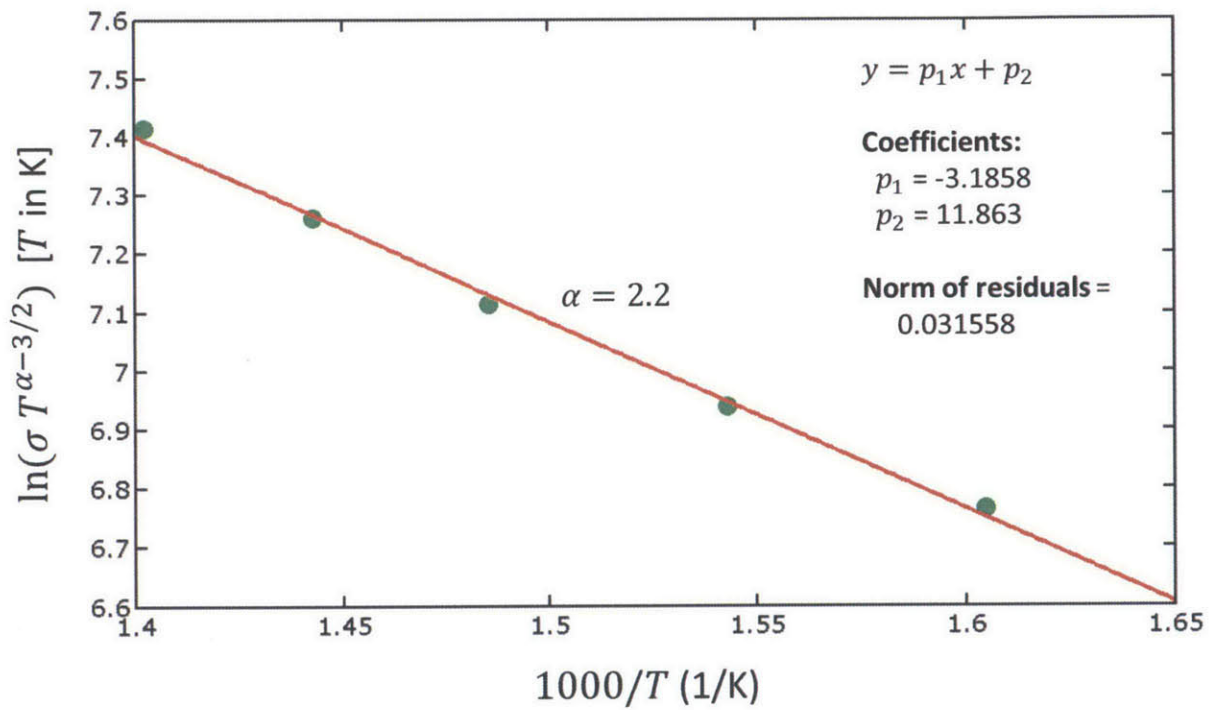Figure B-2: $\mu_{Hall} \propto T^{-\alpha}$ fit for sample N2.

Figure B-3: Conductivity fit according to Eq. (2.11), assuming a $\mu_{Hall} \propto T^{-2.0}$ Hall mobility dependence.
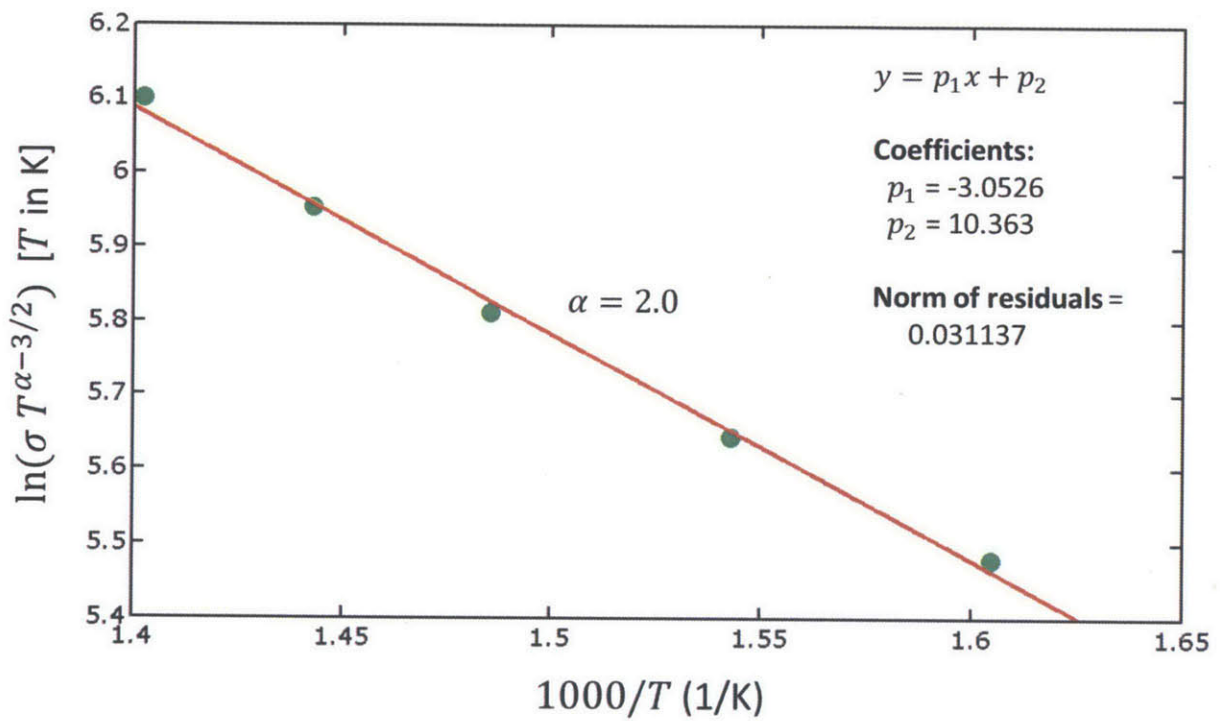
Figure B-4: Conductivity fit according to Eq. (2.11), assuming a $\mu_{Hall} \propto T^{-2.2}$ Hall mobility dependence.

THIS PAGE INTENTIONALLY LEFT BLANK

Bibliography

[1] O. Morton, "Solar energy: a new day dawning? Silicon Valley sunrise.," *Nature*, vol. 443, pp. 19–22, Sept. 2006.

[2] U.S. Energy Information Administration, "Annual energy review," 2011. [Online; accessed 01-January-2014].

[3] First Solar, Inc., "Third quarter 2013: Key financial data," 2013. [Online; accessed 01-January-2014].

[4] B. Schubert, S. Kötschau, H. W. Cinque, and G. M. Schock, "An economic approach to evaluate the range of coverage of indium and its impact on indium based thin-film solar cells - recent results of Cu_2ZnSnS_4 (CZTS) based solar cells," in *Proc. 23rd EU PVSEC*, pp. 3788–3792, 2008.

[5] A. Ennaoui, S. Fiechter, C. Pettenkofer, N. Alonsovante, K. Buker, M. Bronold, C. Hopfner, and H. Tributsch, "Iron disulfide for solar energy conversion," *Solar Energy Materials and Solar Cells*, vol. 29, pp. 289–370, May 1993.

[6] W. Shockley and H. J. Queisser, "Detailed Balance Limit of Efficiency of p-n Junction Solar Cells," *Journal of Applied Physics*, vol. 32, no. 3, p. 510, 1961.

[7] Y. Zhang, J. Hu, M. Law, and R. Wu, "Effect of surface stoichiometry on the band gap of the pyrite $FeS_{2}(100)$ surface," *Physical Review B*, vol. 85, pp. 1–5, Feb. 2012.

[8] P. Lazić, R. Armiento, F. W. Herbert, R. Chakraborty, R. Sun, M. K. Y. Chan, K. Hartman, T. Buonassisi, B. Yildiz, and G. Ceder, "Low intensity conduction states in FeS2: implications for absorption, open-circuit voltage and surface recombination.," *Journal of physics. Condensed matter : an Institute of Physics journal*, vol. 25, p. 465801, Nov. 2013.

[9] G. von Oertzen, W. Skinner, and H. Nesbitt, "Ab initio and x-ray photoemission spectroscopy study of the bulk and surface electronic structure of pyrite (100) with implications for reactivity," *Physical Review B*, vol. 72, p. 235427, Dec. 2005.

[10] A. Abd El Halim, S. Fiechter, and H. Tributsch, "Control of interfacial barriers in n-type FeS2 (pyrite) by electrodepositing metals (Co, Cu) forming isostructural disulfides," *Electrochimica Acta*, vol. 47, pp. 2615–2623, June 2002.

[11] M. Birkholz, S. Fiechter, A. Hartmann, and H. Tributsch, "Sulfur deficiency in iron pyrite (FeS2-x) and its consequences for band-structure models," *Physical Review B*, vol. 43, pp. 11926–11936, May 1991.

[12] M. Bronold, C. Pettenkofer, and W. Jaegermann, "Surface photovoltage measurements on pyrite (100) cleavage planes: Evidence for electronic bulk defects," *Journal of Applied Physics*, vol. 76, no. 10, p. 5800, 1994.

[13] M. Bronold, K. Büker, S. Kubala, C. Pettenkofer, and H. Tributsch, "Surface Preparation of FeS2 via Electrochemical Etching and Interface Formation with Metals," *Physica Status Solidi (a)*, vol. 135, pp. 231–243, Jan. 1993.

[14] Q. Guanzhou, X. Qi, and H. Yuehua, "First-principles calculation of the electronic structure of the stoichiometric pyrite FeS2(100) surface (No. 03-11)," *Computational Materials Science*, vol. 29, pp. 89–94, Jan. 2004.

[15] C. Wadia, Y. Wu, S. Gul, S. K. Volkman, J. Guo, and a. P. Alivisatos, "Surfactant-Assisted Hydrothermal Synthesis of Single phase Pyrite FeS 2 Nanocrystals," *Chemistry of Materials*, vol. 21, pp. 2568–2570, July 2009.

[16] R. Sun, M. Chan, and G. Ceder, "First-principles electronic structure and relative stability of pyrite and marcasite: Implications for photovoltaic performance," *Physical Review B*, vol. 83, pp. 1–12, June 2011.

[17] R. Sun, M. K. Y. Chan, S. Kang, and G. Ceder, "Intrinsic stoichiometry and oxygen-induced p-type conductivity of pyrite FeS_{2}," *Physical Review B*, vol. 84, p. 035212, July 2011.

[18] F. Herbert, a. Krishnamoorthy, K. Van Vliet, and B. Yildiz, "Quantification of electronic band gap and surface states on FeS2(100)," *Surface Science*, vol. 618, pp. 53–61, Dec. 2013.

[19] K. Sato, "Reflectivity Spectra and Optical Constants of Pyrites (FeS 2 , CoS 2 and NiS 2) between 0.2 and 4.4 eV," *Journal of the Physics Society Japan*, vol. 53, pp. 1617–1620, May 1984.

[20] A. Schlegel and P. Wachter, "Optical properties, phonons and electronic structure of iron pyrite (FeS 2)," *Journal of Physics C: Solid State Physics*, vol. 9, pp. 3363–3369, Sept. 1976.

[21] S. Suga, K. Inoue, M. Taniguchi, S. Shin, M. Seki, K. Sato, and T. Teranishi, "Vacuum Ultraviolet Reflectance Spectra and Band Structures of Pyrites (FeS 2 , CoS 2 and NiS 2) and NiO Measured with Synchrotron Radiation," *Journal of the Physics Society Japan*, vol. 52, pp. 1848–1856, May 1983.

[22] T. A. Bither, R. J. Bouchard, W. H. Cloud, P. C. Donohue, and W. J. Siemons, "Transition metal pyrite dichalcogenides. High-pressure synthesis and correlation of properties," *Inorganic Chemistry*, vol. 7, pp. 2208–2220, Nov. 1968.

[23] J. I. Pankove, "Absorption," in *Optical processes in semi-conductors*, pp. 34–43, DoverPublications.com, 1971.

[24] T.-R. Yang, J.-T. Yu, J.-K. Huang, S.-H. Chen, M.-Y. Tsay, and Y.-S. Huang, "Optical-absorption study of synthetic pyrite FeS2 single crystals," *Journal of Applied Physics*, vol. 77, no. 4, p. 1710, 1995.

[25] A. M. Karguppikar and A. G. Vedeshwar, "Electrical and optical properties of natural iron pyrite (FeS2)," *Physica Status Solidi (a)*, vol. 109, pp. 549–558, Oct. 1988.

[26] W. Kou and M. Seehra, "Optical absorption in iron pyrite (FeS_{2})," *Physical Review B*, vol. 18, pp. 7062–7068, Dec. 1978.

[27] I. Ferrer, D. Nevskaia, C. de las Heras, and C. Sánchez, "About the band gap nature of FeS2 as determined from optical and photoelectrochemical measurements," *Solid State Communications*, vol. 74, pp. 913–916, June 1990.

[28] R. Schieck, A. Hartmann, S. Fiechter, R. Könenkamp, and H. Wetzel, "Electrical properties of natural and synthetic pyrite (FeS2) crystals," *Journal of Materials Research*, vol. 5, pp. 1567–1572, Jan. 1990.

[29] G. Willeke, O. Blenk, C. Kloc, and E. Bucher, "Preparation and electrical transport properties of pyrite (FeS2) single crystals," *Journal of Alloys and Compounds*, vol. 178, pp. 181–191, Feb. 1992.

[30] O. Blenk, E. Bucher, and G. Willeke, "P-Type Conduction in Pyrite Single Crystals Prepared By Chemical Vapor Transport," *Applied Physics Letters*, vol. 62, no. 17, p. 2093, 1993.

[31] C. Kloc, G. Willeke, and E. Bucher, "Flux growth and electrical transport measurements of pyrite (FeS2)," *Journal of Crystal Growth*, vol. 131, pp. 448–452, Aug. 1993.

[32] M. Morsli, A. Bonnet, L. Cattin, A. Conan, and S. Fiechter, "Electrical Properties of a Synthetic Pyrite FeS 2 Non Stoichiometric Crystal," *Journal de Physique I*, vol. 5, pp. 699–705, June 1995.

[33] T. Harada, "Transport Properties of Iron Dichalcogenides FeX 2 (X=S, Se and Te)," *Journal of the Physics Society Japan*, vol. 67, pp. 1352–1358, Apr. 1998.

[34] C. Ho, Y. Huang, and K. Tiong, "Characterization of near band-edge properties of synthetic p-FeS2 iron pyrite from electrical and photoconductivity measurements," *Journal of Alloys and Compounds*, vol. 422, pp. 321–327, Sept. 2006.

[35] J. Marinace, "Some Electrical Properties of Natural Crystals of Iron Pyrite," *Physical Review*, vol. 96, pp. 593–593, Nov. 1954.

[36] H. Horita, "Electrical Properties of Natural Pyrite between 1.3 and 700K," *Japanese Journal of Applied Physics*, vol. 10, pp. 1478–1479, Oct. 1971.

[37] H. Horita, "Some Semiconducting Properties of Natural Pyrite," *Japanese Journal of Applied Physics*, vol. 12, pp. 617–618, Apr. 1973.

[38] A. Echarri and C. Sánchez, "n type semiconductivity in natural single crystals of FeS2 (pyrite)," *Solid State Communications*, vol. 15, pp. 827–831, Sept. 1974.

[39] P. Waldner and a.D. Pelton, "Thermodynamic Modeling of the Fe-S System," *Journal of Phase Equilibria & Diffusion*, vol. 26, pp. 23–38, Feb. 2005.

[40] P. Blood and J. W. Orton, "The electrical characterisation of semiconductors," *Reports on Progress in Physics*, vol. 41, pp. 157–257, Feb. 1978.

[41] L.J. van der Pauw, "A Method of Measuring the Resistivity and Hall Coefficient on Lamellae of Arbitrary Shape," 1958.

[42] M. T. Winkler, *Non-Equilbrium Chalcogen Concentrations in Silicon : Physical Structure , Electronic Transport , and Photovoltaic Potential.* PhD thesis, Harvard University, 2009.

[43] J. Dorkel and P. Leturcq, "Carrier mobilities in silicon semi-empirically related to temperature, doping and injection level," *Solid-State Electronics*, vol. 24, pp. 821–825, Sept. 1981.

[44] M. Wakihara, J. Nii, T. Uchida, and M. Taniguchi, "Calculation of Partial Pressures on Each Sulfur Species in Total Sulfur Vapor at Temperatures From 350C to 1000C Under One Atmospheric Pressure," *Chemistry Letters*, vol. 6, pp. 621–626, 1977.

[45] D. J. Vaughan and J. R. Craig, "Sulfide Phase Equilibria," in *Mineral chemistry of metal sulfides*, pp. 285–287, Cambridge University Press, 1978.

[46] A. Ennaoui, S. Fiechter, H. Goslowsky, and H. Tributsch, "Photoactive Synthetic Polycrystalline Pyrite (FeS[sub 2])," *Journal of The Electrochemical Society*, vol. 132, no. 7, p. 1579, 1985.

[47] D. M. Roessler, "Kramers-Kronig analysis of reflection data," *British Journal of Applied Physics*, vol. 16, pp. 1119–1123, Aug. 1965.

[48] N. M. Ravindra and V. K. Srivastava, "Temperature dependence of the energy gap in pyrite (FeS2)," *Physica Status Solidi (a)*, vol. 65, pp. 737–742, June 1981.